

Measurement and prediction of ultralow frequency ocean ambient noise off the eastern U.S. coast

D. Keith Wilson,^{a)} George V. Frisk, Timothy E. Lindstrom,^{b)} and Cynthia J. Sellers
*Department of Applied Ocean Physics and Engineering, Woods Hole Oceanographic Institution,
Woods Hole, Massachusetts 02543*

(Received 13 December 2001; revised 29 January 2003; accepted 31 January 2003)

Ultralow frequency (0.02–2 Hz) acoustic ambient noise was monitored from January to April 1991 at six ocean bottom stations off the eastern U.S. coast. The depths of the stations ranged from about 100 m to 2500 m. The measured spectra are in good agreement with predictions made using Cato's theory [J. Acoust. Soc. Am. **89**, 1076–1095 (1991)] for noise generation by surface-wave orbital motion after extending the calculations to incorporate horizontally stratified environments. Contributions from both the linear, single-frequency (virtual monopole) and the nonlinear, double-frequency (dipole) mechanisms are clearly recognizable in the data. The predictions make use of directional wave data obtained from surface buoys deployed during the SWADE experiment and an ocean bottom model derived from compressional wave speed data measured during the EDGE deep seismic reflection survey. The results demonstrate conclusively that nonlinear surface-wave interactions are the dominant mechanism for generating deep-ocean ULF noise in the band 0.2–0.7 Hz. © 2003 Acoustical Society of America. [DOI: 10.1121/1.1568941]

PACS numbers: 43.30.Nb, 43.30.Lz [DLB]

I. INTRODUCTION

This paper presents results from ECONOMEX, the Environmentally Controlled Ocean-floor NOise Monitoring EXperiment. The overall purpose of ECONOMEX was to study the variability, both with respect to depth and time, of ULF/VLF (0.001–10 Hz) ambient noise in a continental margin region. Six ONR Ocean Bottom Seismometers (OBS's), equipped with differential pressure gauges (DPG's) and three-component seismometers, were deployed from January to April 1991. The sensors were placed off the Virginia coastline in water depths ranging from 95 m to 2600 m.

A more specific goal of the experiment was to determine conclusively whether ULF/VLF noise in the ocean (particularly at deep sites), and the associated seismic activity known as microseisms, are generated by nonlinear interactions of ocean surface waves. It has long been understood that an evanescent pressure wave exists under ocean surface waves, having frequency equal to the surface waves. The seismic waves generated by these pressure disturbances are referred to as *single-frequency microseisms*. Because of its evanescent nature, however, the single-frequency mechanism cannot be the cause of typical ULF/VLF noise levels observed at deep ocean sites. Recognizing this fact, Longuet-Higgins¹ proposed one-half century ago that the primary source of ULF/VLF noise in the deep ocean is a nonlinear interaction between opposing surface wavetrains, which produces a non-evanescent pressure disturbance in the ocean at a frequency twice that of the ocean surface waves. The resulting seismic activity is known as *double-frequency microseisms*.

More recently, Cato^{2,3} developed a comprehensive theory, based on Lighthill's analogy, for ocean noise genera-

tion by the sea-surface motions. The single-frequency noise field is associated with a time-varying mass flux at the surface, which radiates sound as a distribution of virtual monopoles. The double-frequency noise field is associated with a time-varying momentum flux at the surface, which radiates sound as a distribution of virtual dipoles.

Since the mid-1980s, many authors^{3–13} have provided good experimental evidence in support of the Longuet-Higgins theory. (See also the recent review article by Webb.¹⁴) Most of the initial studies (Refs. 4–8) relied on surface wave spectra estimated from mean wind speed measurements. Kibblewhite and Ewans,⁹ however, made simultaneous measurements of seismic waves and surface wave height spectra in 100 m of water. A study by Cato³ involved simultaneous measurements of noise and surface wave height spectra in a lake. More recently, Babcock *et al.*,¹⁰ Nye and Yamamoto,¹¹ Herbers and Guza,¹² and Tindle and Murphy¹³ performed simultaneous measurements of microseisms and surface wave height spectra in the open ocean. We note that the work described in Refs. 10–12 was part of the ONR Sources of Ambient Microseismic Ocean Noise (SAMSON) experiment, which was conducted in October to November 1990 off the coast of North Carolina.

ECONOMEX, which followed shortly after SAMSON, provided oceanfloor noise measurements in the band 0.02–2 Hz at a wide range of depths over several months. Excellent supporting environmental data were also available. Surface-wave directional spectra were recorded concurrently as part of the SWADE (Surface WAVE Dynamics Experiment) project.¹⁵ These data are the essential environmental control needed to test Cato's theory. SWADE also provided meteorological data such as wind speed and direction. In addition to the surface-wave directional spectra, accurate modeling of ULF/VLF noise in the ocean requires profiles of compressional and shear wave speeds deep into the Earth's crust. In this regard, ECONOMEX benefitted from the availability of deep seismic profiles determined during the EDGE survey.¹⁶

^{a)}Present address: U.S. Army Cold Regions Research Laboratory, CEERD-RC, 72 Lyme Rd., Hanover, NH 03755-1290.

^{b)}Present address: Commander, Submarine Squadron 20, 1050 USS Georgia Avenue, Kings Bay, GA 31547

ECONOMEX and SWADE instrument locations

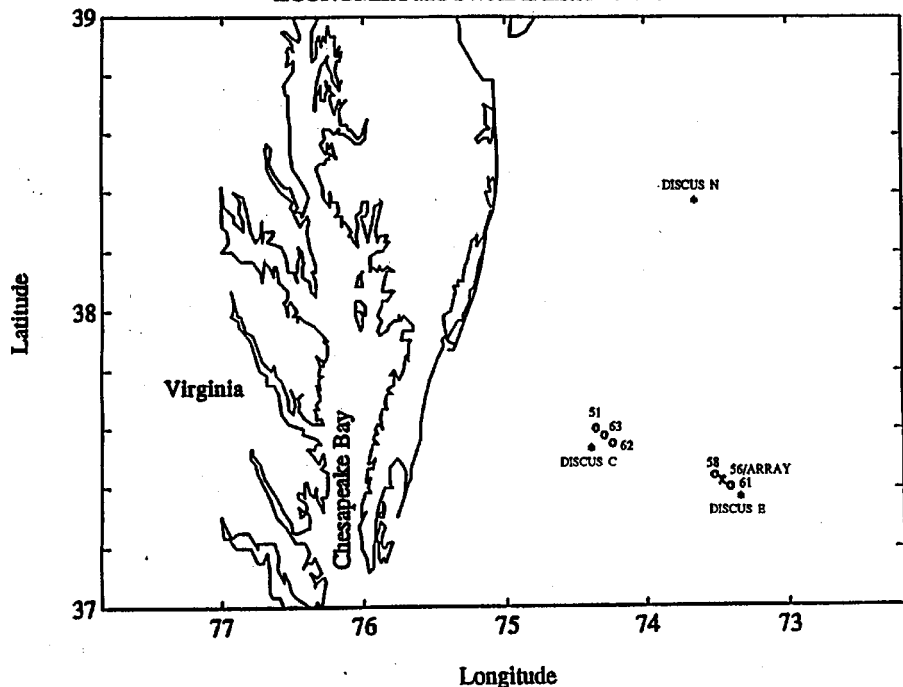


FIG. 1. Approximate locations of the ECONOMEX and relevant SWADE instruments. “*” denotes pitch and roll buoy location, “x” denotes location of one ONR ocean bottom seismometer (OBS) and two hydrophone arrays, and “o” denotes the location of one ONR OBS.

Using the EDGE data, we are able to estimate the compressional and shear wave speed profiles to depths of 10 km, and then incorporate these profiles into a noise prediction model.

The format of the paper is as follows. In Sec. II, we discuss the ECONOMEX data set and the environmental inputs (the SWADE and EDGE data) used by our noise prediction model. Our predictive model for the ULF/VLF spectra, which is based on Cato’s theory,^{2,3} is described in Sec. III. Last, in Sec. IV, seafloor pressure spectra from ECONOMEX are compared to the model, with special attention given to the relationship between changing wave height conditions and the double-frequency noise field.

II. EXPERIMENT

A. ECONOMEX deployments

ECONOMEX was designed to provide a long-term, high-quality, seismo-acoustic data set that could be coupled to the surface wave and meteorological data of the SWADE experiment. The instrumentation consisted of six Office of Naval Research (ONR) ocean bottom seismometers (OBS’s) and two (one vertical and one horizontal) 75 m, six-element hydrophone arrays. The instruments were deployed off the Virginia coast in January 1991, recovered in February 1991 for maintenance, and redeployed from February through

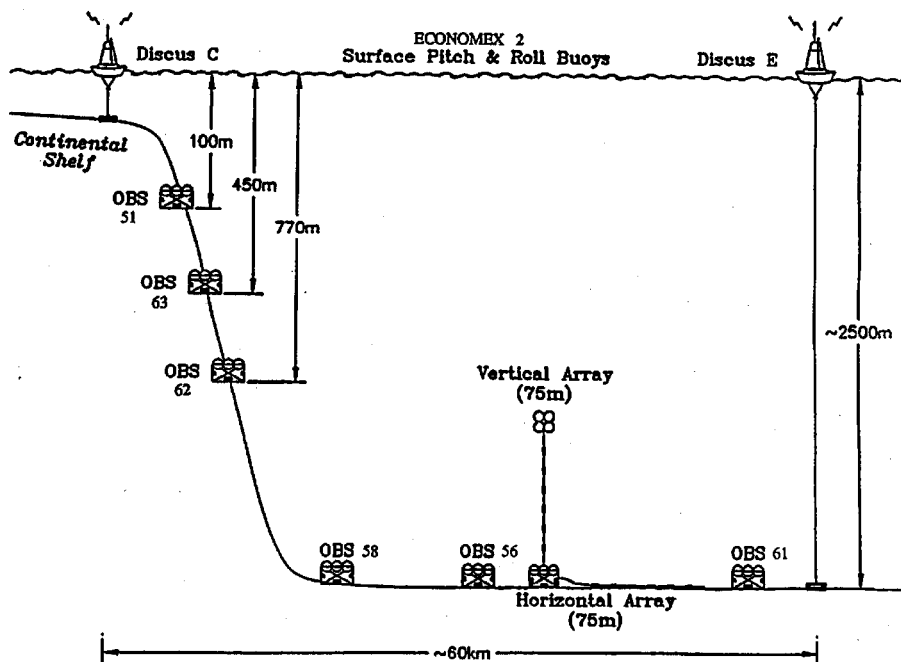


FIG. 2. Schematic arrangement of ECONOMEX and SWADE deployments.

TABLE I. Locations of the ECONOMEX instruments. Positions and depths listed are for the second leg of the experiment; those for the first leg differ only slightly. Also note OBS frames 61 and 62 exchanged positions between the first and second legs, although the instruments on them were exchanged also such that the instruments remained deployed in the same locations.

Instrument name	Lat.	Long.	Depth (m)	Deployment dates (1991)
Vert. array	37° 24.7' N	73° 26.8' W	2573	25 Jan–6 Feb; 22 Feb–5 Apr
Horz. array	37° 24.7' N	73° 26.8' W	2573	25 Jan–6 Feb; 22 Feb–5 Apr
OBS 56	37° 24.7' N	73° 26.8' W	2548	25 Jan–6 Feb; 22 Feb–5 Apr
OBS 58	37° 26.4' N	73° 31.4' W	2417	24 Jan–7 Feb; 22 Feb–5 Apr
OBS 61	37° 23.8' N	73° 24.4' W	2600	25 Jan–6 Feb; 21 Feb–4 Apr
OBS 62	37° 33.2' N	74° 14.1' W	769	11 Jan–6 Feb; 22 Feb–5 Apr
OBS 63	37° 34.1' N	74° 16.5' W	443	10 Jan–6 Feb; 22 Feb–5 Apr
OBS 51	37° 35.9' N	74° 21.3' W	95	10 Jan–6 Feb; 22 Feb–5 Apr

early April 1991. The instrument locations are shown schematically in Figs. 1 and 2. Precise locations and deployment dates are listed in Table I.

The deployed ONR OBS instruments consisted of a three-component geophone for measuring ground motion in the 0.07 to 80 Hz range, a Cox–Webb differential pressure gauge (DPG) for measuring long-period pressure signals in the water column, and in the original deployment, an OAS hydrophone.¹⁸ In the later deployment, these hydrophones were removed to improve instrument reliability.

The sensors were connected via preamplifiers to an acquisition package consisting of a prewhitening and antialiasing filter, a gain-ranging amplifier to improve dynamic range, and an analog-to-digital converter. The combined filter response is shown in Fig. 3. The acquisition package fed a recording unit consisting of a RAM buffer and an optical disc recording system capable of storing 400 megabytes of data. Most of the OBS's were programmed for continuous 8 Hz recording, with the antialiasing filter set to 2 Hz; however, one of the devices (OBS 56) was set to record at 128 Hz with its antialiasing filter set to 40 Hz.

The 75 m horizontal and vertical arrays each consisted of six OAS hydrophones at 15 m separation. The hydrophone signals were preamplified by a low-noise, wide-range preamplifier and sent to acquisition and recording packages identical to those of the OBS's, with 128 Hz sampling and

the antialiasing filter set to 40 Hz. In the second deployment the bottom three hydrophones of the vertical array were not included due to a cable malfunction. The array cable jacket included loose ended fiber strands to reduce strumming noise.

B. ECONOMEX DPG time series and processing

The focus of this paper is on the DPG time series. Power spectra from these data were computed by partitioning the overall time series into records of 4096 samples, each having 512 s (8.5 min) duration. The responses of the prewhitening and antialiasing filter were then removed from each record. The results, for the entire second observational period of ECONOMEX, are shown in the upper panels of Figs. 4–7. These figures are for OBS 51 (95 m depth), OBS 63 (443 m depth), OBS 62 (769 m depth), and OBS 61 (2600 m depth), respectively. (The gaps in these figures are intervals when data were not acquired.)

The spectra are observed to have a strong depth dependence. Sound pressure levels at the shallowest sensor (OBS 51), in the frequency band 0.06–0.12 Hz, are in the range 150–170 dB *re* 1 (μPa)²/Hz. These are the highest levels recorded at any of the sensors. In roughly the same band, the sound levels recorded by the sensors at the greater depths were all between 70 and 90 dB.

At the next shallowest sensor (OBS 63), levels in the range 120–130 dB are evident below 0.06 Hz. Comparable levels are evident at OBS 62, below 0.04 Hz. No such low frequency energy is evident at the deepest sensor (OBS 61), at least for the frequency range displayed on the spectral plots. The spectral energy below about 0.12 Hz can be confidently attributed to the single-frequency noise field, for which the spectral energy decays exponentially with increasing depth and frequency. As the sensor depth is increased, higher frequencies are unable to penetrate to the bottom.

At the deepest sensor (OBS 61, 2600 m), most of the spectral energy lies in the band 0.2–0.5 Hz. The levels exhibit considerable temporal variability, fluctuating between about 110 and 145 dB. As will become evident when we examine the surface-buoy data, the variability in the pressure field at OBS 61 strongly parallels variations in wave-height power spectrum occurring at one-half the acoustic frequency. The spectral energy in this band must therefore be the double-frequency generation mechanism created by nonlin-

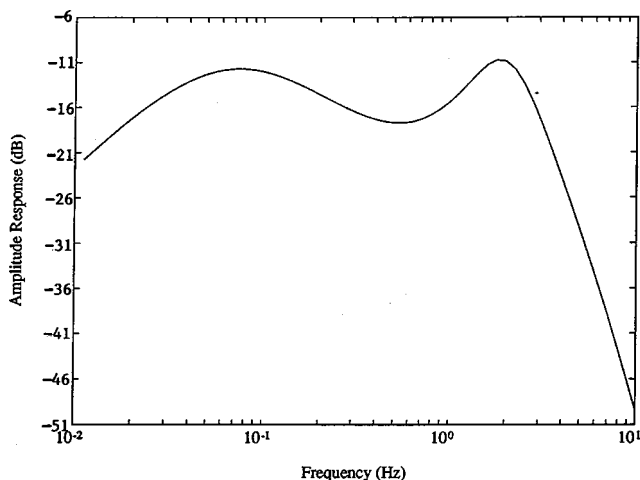


FIG. 3. Amplitude response of the antialiasing and prewhitening filter used in the ECONOMEX instruments with an 8 Hz sampling rate. Response amplitude in dB *re* 1 V.

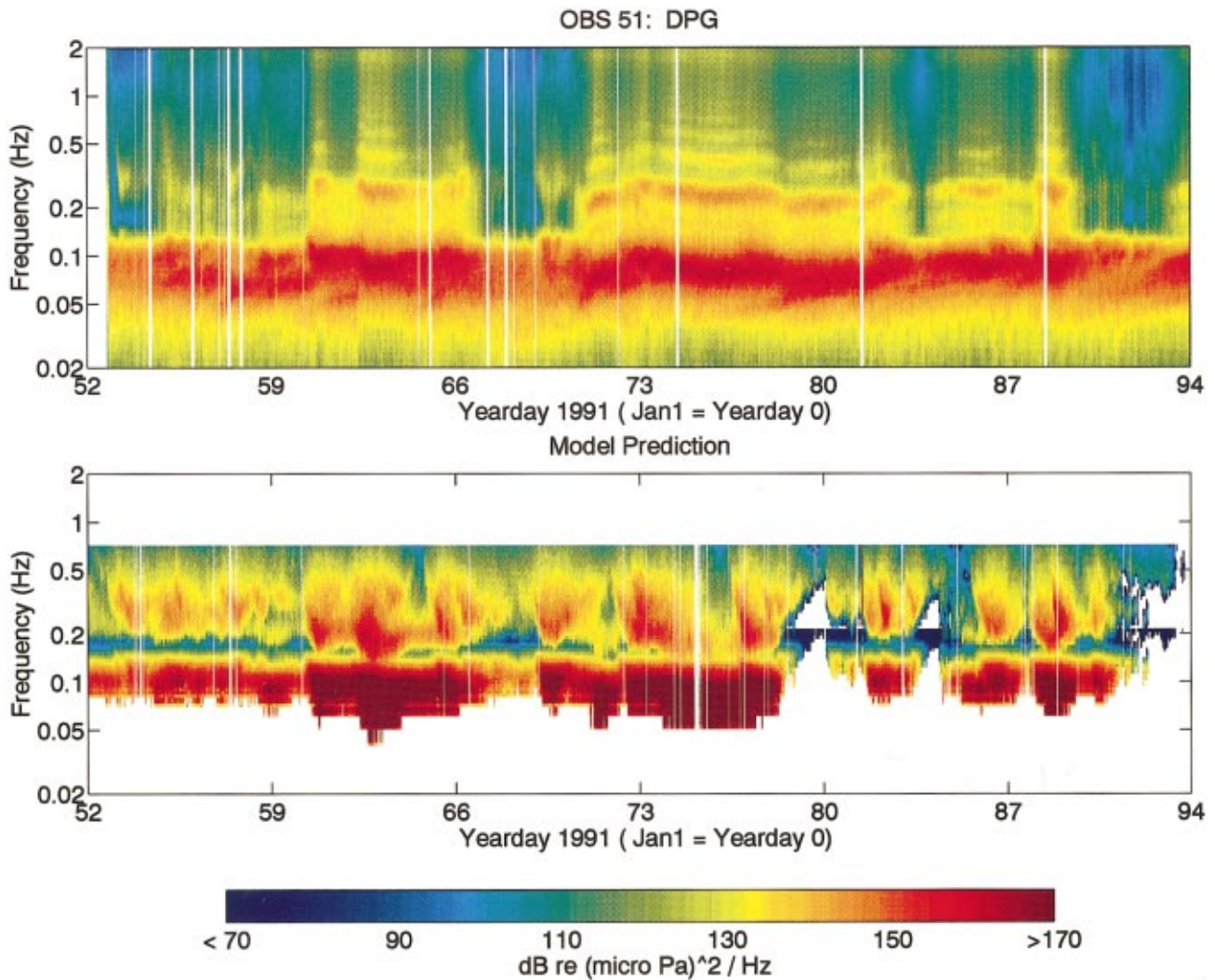


FIG. 4. Differential pressure gauge (DPG) power spectral levels for OBS 51 (95 m depth), second deployment. Upper, measurement. Lower, model prediction.

ear interaction of opposing wavetrains, as was first suggested by Longuet-Higgins.¹ The double-frequency noise, including as it does a nonevanescent component (i.e., a component that does not attenuate with increasing depth), is strong at the deepest sensor, whereas the single-frequency noise, which is evanescent, is not observed there. The nonevanescent nature of the double-frequency noise also explains why it is evident at the other OBS's with approximately the same strength. At OBS 63 and 62 (443 and 769 m), a spectral gap is evident between the single- and double-frequency noise. The gap is not present at OBS 51, since higher frequencies attributable to single-frequency pressure disturbances are able to penetrate to its relatively shallow depth of 95 m. We will develop a quantitative model for these effects in Sec. III.

C. Supporting data

1. SWADE surface wave spectra

The SWADE project was an effort to characterize the sea surface using a variety of sensors and, at the same time, measure other relevant environmental parameters.¹⁵ The project included several pitch and roll surface buoys, satellite radar backscatter measurements, SWATH ship array deployments, and aircraft overflights. The long-term deployment of

the pitch-and-roll buoys is the element of the experiment of direct use in our effort to predict noise generated by surface wave motion. In particular, the buoys were used to determine the surface-wave directional spectra required by our noise prediction model. Collection and processing of the SWADE data are discussed in this section.

The SWADE instrument locations are shown together with the ECONOMEX instruments in Figs. 1 and 2. Precise deployment locations of SWADE instruments are listed in Table II. The buoys provided one complete set of measurements (including a spectral estimate) each hour, allowing us to update our estimate of the noise field each hour. The SWADE buoys that were closest to the ECONOMEX instruments were Discus C and Discus E. Figure 8 shows wind speed, time rate-of-change of wind direction, and the wave height power spectrum from Discus E for the duration of ECONOMEX. Periods of elevated activity lasting typically 2–3 days are clearly evident in the spectra. These usually correspond to mid-latitude cyclonic activity in the atmosphere (storms).

The wave-height spectral data from the SWADE buoys were provided for frequencies from 0.03 Hz to 0.34 Hz, in 0.01 Hz bins. For predicting the noise at the deep

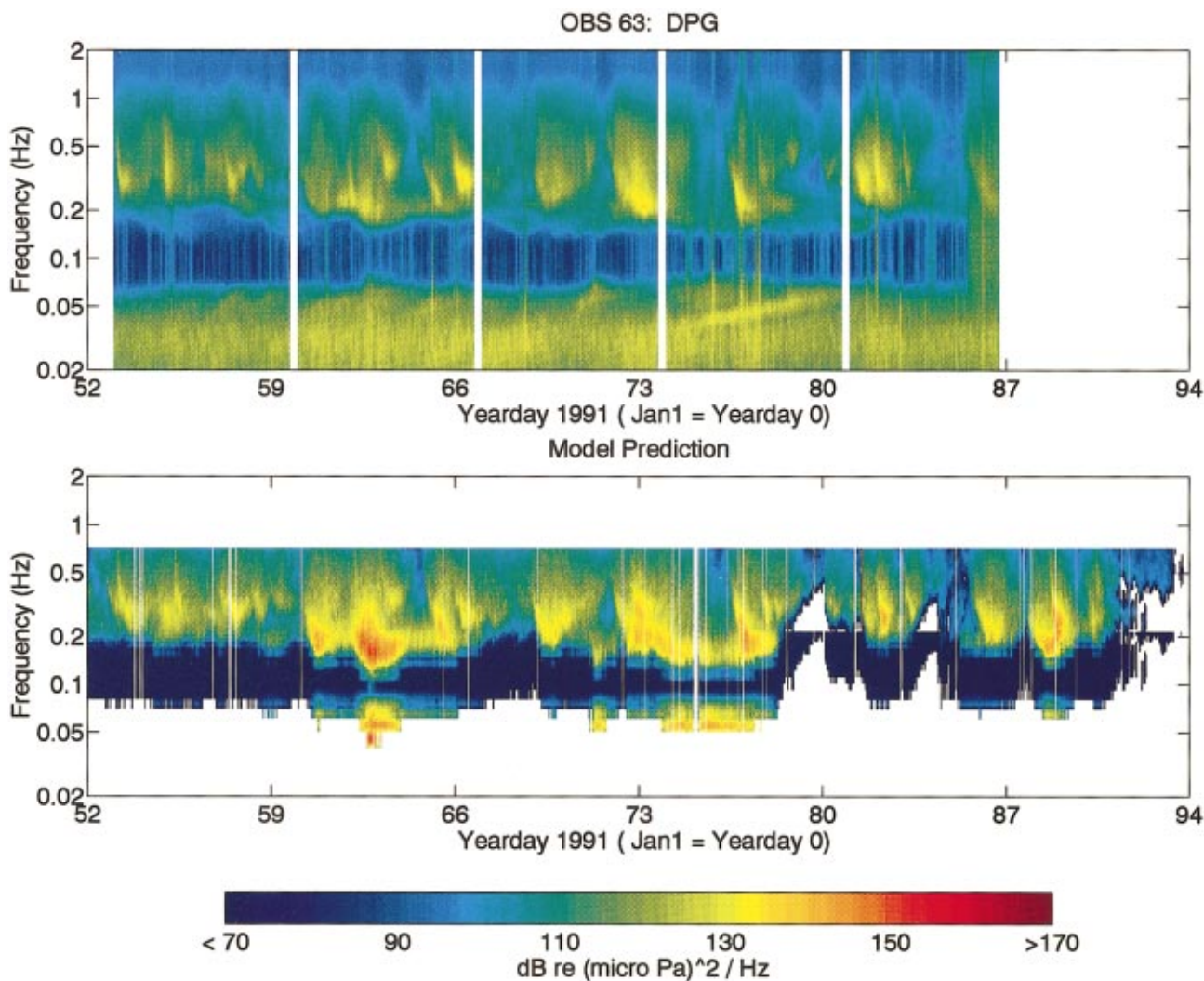


FIG. 5. DPG power spectral levels for OBS 63 (443 m depth), second deployment. Upper, measurement. Lower, model prediction.

ECONOMEX site, the data from Discus E were used, while predictions of noise at the three shallowest ECONOMEX instruments were based on data from Discus C. SWADE had also deployed a SPAR buoy (which had better angular resolution than the Discus buoys) near the shallow ECONOMEX site, but it sank prior to the ECONOMEX deployments.

As is well known, ocean surface waves are dispersive, with the relationship depending on water depth. We should therefore consider the possible effect of using a surface buoy moored in 95 m of water (Discus C) to predict noise at the 443 m and 769 m OBS's. First we note from the measured wave spectra that there is little energy below 0.1 Hz in the wave spectrum. If we calculate $\tanh(kd)$ (the depth-dependent factor of the surface-wave dispersion relation) for the worst case of 0.1 Hz with $d=95$ m, we find the dispersion factor to be less than 1%. Thus any corrections to the wave spectra measured at Discus C for the 443 m and 769 m OBS's are quite small.

Pitch-and-roll buoys, such as the Discus buoys, can provide only an estimate of the surface-wave directional spectrum. Because our ULF/VLF noise prediction model (Sec. III) depends strongly on the directional spectrum, the method used to estimate the spectrum takes on critical importance.

The case of particular interest is when the wind direction changes rapidly in time, creating opposing wavetrains on the sea surface. This situation causes the spreading integral (required for predictions of the double-frequency noise field) to be large. Among the many methods available we have considered are empirical estimates, the Longuet-Higgins *et al.*¹⁷ method, maximum-likelihood (MLM) estimates, and maximum-entropy (MEM) estimates. The reader is referred to the Appendix for a more detailed discussion of our procedures for making the wave-directional estimates.

The four methods of wave-directional spectral estimation are compared in Fig. 9. A simulated bi-directional spectrum was the input. In Fig. 10 we compare estimates of the directional spectra for an actual datum from SWADE: the 0.16 Hz bin from Discus E at 1200 on 27 January 1991. This datum was chosen as illustrative because it occurs after a shift in wind direction, and one would expect the true spectrum to be bi-directional in this case. One can see from the two figures that MEM is most satisfactory in reproducing a sharply peaked, bi-directional distribution. In fact, a bi-directional structure is evident only in the MEM estimate in Fig. 10. Hence we decided to use MEM for our estimates of the wave-directional spectrum.

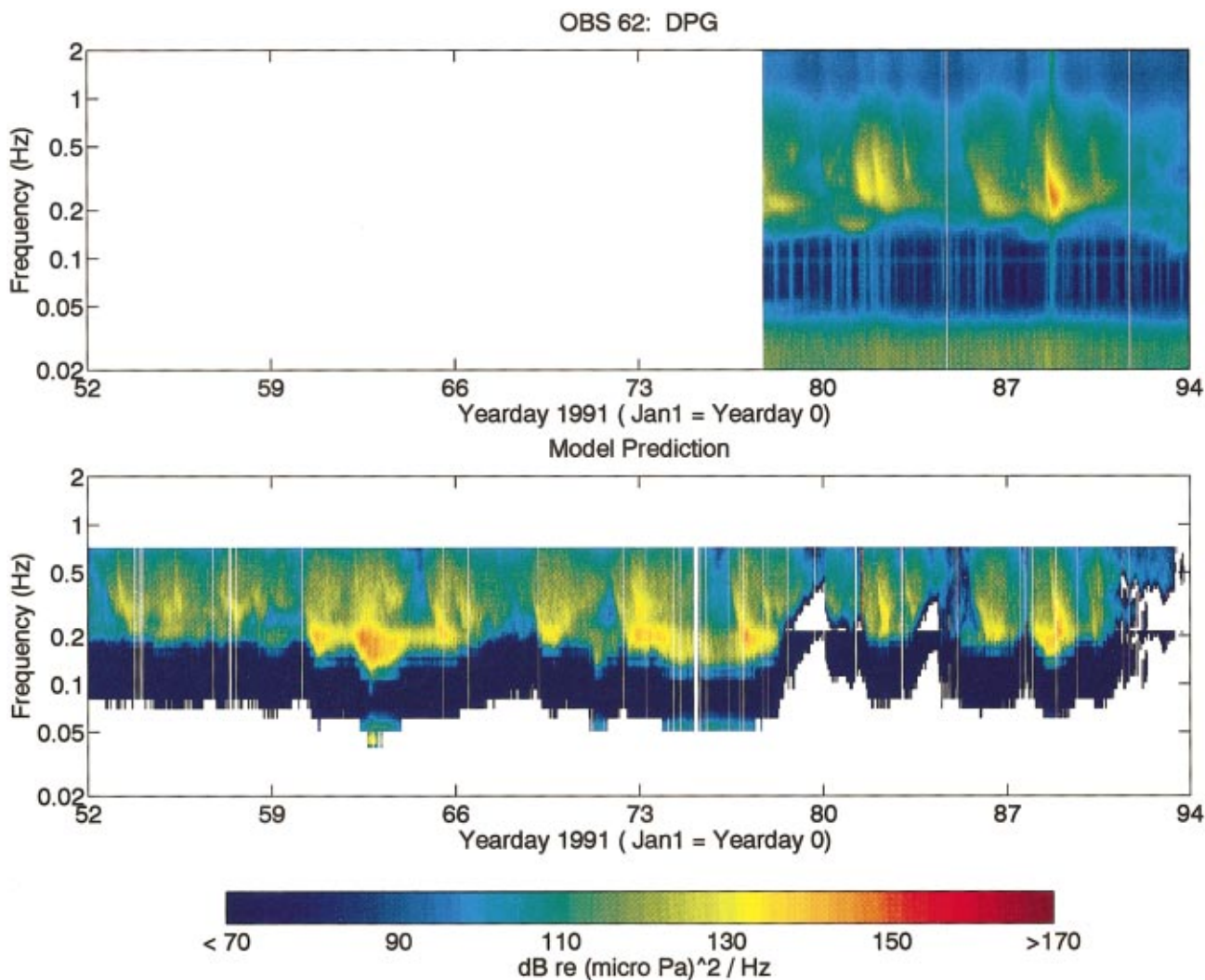


FIG. 6. DPG power spectral levels for OBS 62 (769 m depth), second deployment. Upper, measurement. Lower, model prediction.

2. EDGE profiles

In this section, we discuss our procedure for determining the vertical profiles of the compressional wave speed, shear wave speed, compressional and shear attenuations, and density, as required for input to our noise propagation model. Due to the long wavelengths involved at the very low frequencies of the predictions, the environmental model needs to be as accurate as possible deep into the earth's crust.

As described in the next section, the propagation model is formulated for a horizontally stratified environment. The environment is partitioned into several layers, each having constant seismic properties. The uppermost layer, actually a semi-infinite half space, is the air layer, represented by a vacuum in our model. The next layer down, the water layer, is assumed to have a constant sound speed of 1500 m/s and constant density of 1000 kg/m³. Approximating the water column as an isovelocity, isodensity layer is quite reasonable for the very low frequencies relevant to the present study.

Below the water layer are 10 to 12 earth layers. Data from a deep seismic reflection study of the U.S. mid-Atlantic continental margin, called EDGE, were used to help determine the seismic profiles. The EDGE experiment¹⁶ involved recording refracted seismic waves of 16 s duration off the

Virginia coast, in the same region as the ECONOMEX and SWADE experiments. But because EDGE provided only compressional wave speed data, we were forced to estimate the shear wave speed, compressional attenuation, shear attenuation, and density profiles. Hamilton's¹⁹ data and equations were used for this purpose, and we also benefitted from discussions with other investigators working in the area of geoacoustic modeling.^{20,21} The resulting profiles for each of the four water depths (95, 443, 769, and 2600 m) are plotted in Fig. 11.

III. THEORY AND CALCULATIONS

Our method for predicting the pressure field generated by surface wave motion is summarized in this section. Based on Cato's theory,² it includes contributions from virtual monopoles and dipoles of all orientations. The surface-distributed monopoles, which are the source of the single-frequency noise field, correspond to a time-varying mass flux across the mean position of the ocean surface. The dipoles, which are the source of the double-frequency noise field, correspond to a time-varying momentum flux.

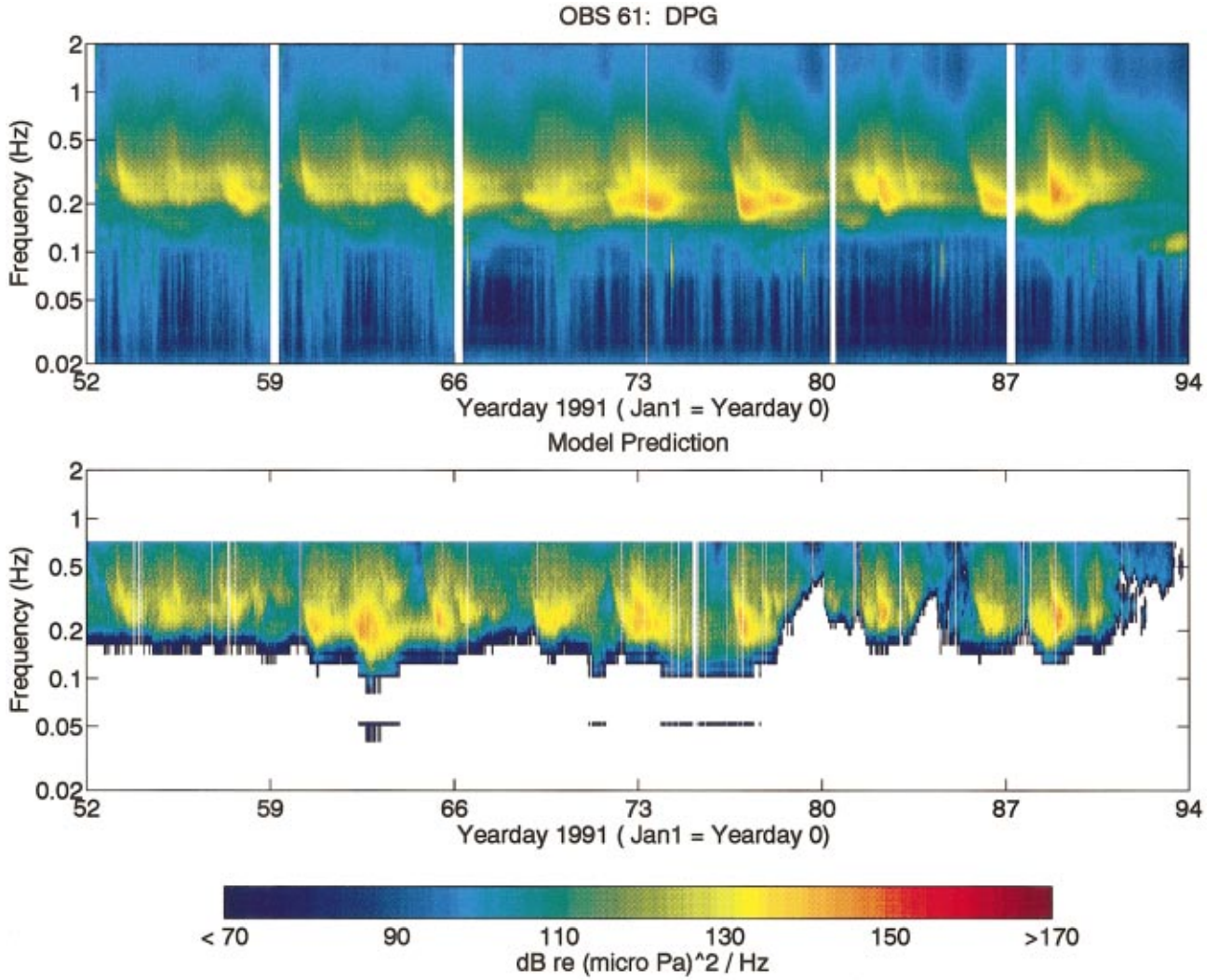


FIG. 7. DPG power spectral levels for OBS 61 (2600 m depth), second deployment. Upper, measurement. Lower, model prediction.

Cato's equation for the double-sided spectral density P_M from the monopoles is

$$P_M(\omega) = \rho^2 c^2 \int_{-\infty}^{\infty} \Psi_{33}(\omega, \mathbf{k}) \times H_0(\omega, \mathbf{k}, z) H_0^*(\omega, \mathbf{k}, z) \frac{d\mathbf{k}}{(2\pi)^2}, \quad (1)$$

where $\omega = 2\pi f$ is the angular frequency, c the sound speed in the water column, \mathbf{k} the horizontal wave number of the surface gravity wave, z the depth, and the superscript asterisk denotes the complex conjugate. The quantity Ψ_{ij} is the cross-spectral density between the velocity components of the surface, u_i and u_j , with subscripts 1 and 2 indicating horizontal axes, and 3 the vertical axis, which originates at

TABLE II. Locations of the SWADE Discus buoys.

Instrument name	Lat.	Long.	Water depth (m)
Discus E	37° 20.0' N	73° 23.5' W	2670
Discus C	37° 32.1' N	74° 23.5' W	102
Discus N	38° 22.1' N	73° 38.9' W	115

the surface and is oriented downward. The quantity H_0 , called the monopole coupling factor, includes the effects of interference, source directivity, and spreading. Specifically, for an infinitely deep, cylindrical ocean of radius R , H_0 is given by [Ref. 2, Eq. (72)]:

$$H_0(\omega, k, z) = \frac{\omega}{2c} \int_0^R \frac{\exp(-i\omega r/c)}{r} J_0(k\hat{r}) \hat{r} d\hat{r}, \quad (2)$$

where $\hat{r}^2 = x^2 + y^2$ is the horizontal displacement, and $r^2 = \hat{r}^2 + z^2$ is the total distance from the source to the receiver.

The dipole contributions P_D are given by [Ref. 2, Eq. (48); also Ref. 3, Eqs. (1) and (A7)]

$$P_{D,ij}(\omega) = \rho^2 \int_{-\infty}^{\infty} [\Phi_{i3j3}(\omega, \mathbf{k}) + \Phi_{i33j}(\omega, \mathbf{k})] \times H_i(\omega, \mathbf{k}, z) H_j^*(\omega, \mathbf{k}, z) \frac{d\mathbf{k}}{(2\pi)^2}, \quad (3)$$

where

$$\Phi_{ij\ell m}(\omega, \mathbf{k}) = \Psi_{i\ell}(\omega, \mathbf{k}) * \Psi_{jm}(\omega, \mathbf{k}), \quad (4)$$

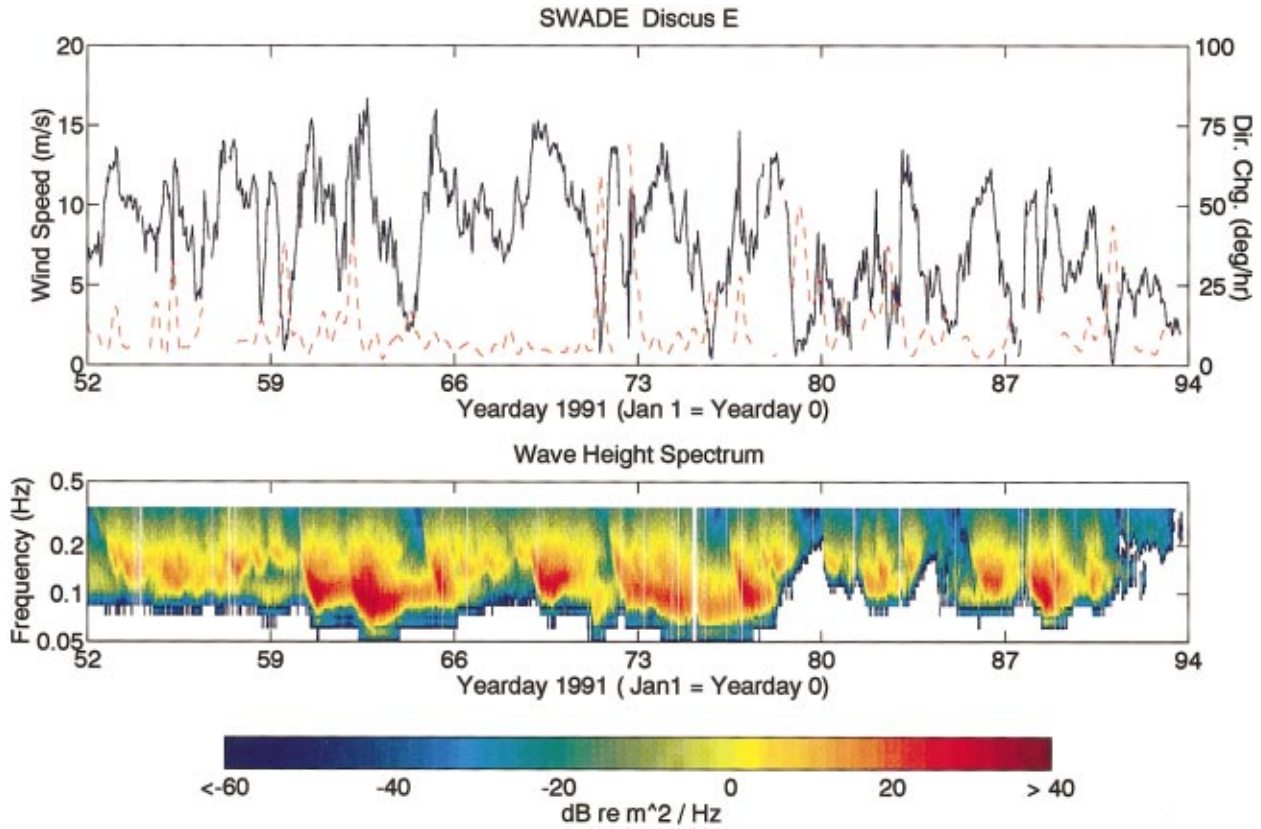


FIG. 8. Data from SWADE Discus E buoy, during the time period of ECONOMEX second deployment. Upper, wind speed (solid line) and rate-of-change of wind direction (dashed line). Lower, wave height power spectrum.

with the asterisk denoting convolution in both frequency and wave number. [No sum over repeated indices is implied in Eq. (3).] The dipole coupling factors are

$$H_1(\omega, \mathbf{k}, z) = -i(kc/\omega)\cos\alpha H_0(\omega, k, z), \quad (5)$$

$$H_2(\omega, \mathbf{k}, z) = -i(kc/\omega)\sin\alpha H_0(\omega, k, z), \quad (6)$$

$$H_3(\omega, \mathbf{k}, z) = \frac{c}{\omega} \frac{\partial}{\partial z} H_0(\omega, k, z), \quad (7)$$

where $\mathbf{k} = (k_x, k_y) = (k \cos \alpha, k \sin \alpha)$.

Using the surface-wave dispersion relation, Eq. (3) can be reduced to³

$$P_{D,ij}(\omega) \approx \pi \rho^2 \left[\frac{\hat{\omega}^4}{\hat{k}} \frac{d\hat{\omega}}{dk} \Omega^2(\hat{\omega}) \right]_{\hat{\omega}=|\omega/2|} \times I_{ij}(|\omega/2|) K_{ij}(|\omega, z|), \quad (8)$$

where

$$I_{ij}(\omega) = \int_0^{2\pi} G(\omega, \alpha) G(\omega, \pi + \alpha) \times |h_i(\hat{k}(\omega), \alpha)| |h_j[\hat{k}(\omega), \alpha]| d\alpha \quad (9)$$

is called the surface-wave *spreading integral*, $\Omega(\omega)$ is the surface-wave-height power spectrum, $G(\omega, \alpha)$ is the surface-wave directionality function, $\hat{k}(\omega)$ is the wave number satisfying the surface-wave dispersion relation ω^2

$$= g\hat{k} \tanh \hat{k}h, \quad h_1(k, \alpha) = i \cos \alpha \coth(kh), \quad h_2(k, \alpha) = i \sin \alpha \times \coth(kh), \quad h_3(k, \alpha) = 1, \quad \text{and}$$

$$K_{ij}(\omega, z) = \int_{-\infty}^{\infty} H_i(\omega, \mathbf{k}, z) H_j^*(\omega, \mathbf{k}, z) \frac{d\mathbf{k}}{(2\pi)^2} \quad (10)$$

is called the *coupling integral*. Working with the definitions of the dipole coupling factors, Eqs. (5)–(7), it is not difficult to show that

$$K_{11}(\omega, z) = K_{22}(\omega, z) = \frac{c^2}{2\omega^2} \int_0^{\infty} H_0(\omega, k, z) H_0^*(\omega, k, z) \frac{k^3 dk}{2\pi}, \quad (11)$$

$$K_{33}(\omega, z) = \int_0^{\infty} H_3(\omega, k, z) H_3^*(\omega, k, z) \frac{k dk}{2\pi}, \quad (12)$$

and $K_{ij} = 0$ if $i \neq j$. Hence only the virtual dipoles having $i = j$ contribute to the pressure field, and the total dipole field is given by $P_D = P_{D,11} + P_{D,22} + P_{D,33}$.

Accurate calculations of the spreading integral, Eq. (9), are difficult to achieve in practice. Recall from Sec. II C 1 that we use a maximum-entropy method (MEM) to attempt to improve spreading-integral calculations derived from pitch-and-roll buoys.

Because the ocean bottom can significantly affect the propagation of sound waves in the water column, even particularly at ULF/VLF frequencies, it is worthwhile to extend Cato's analysis to the case of a horizontally stratified ocean and seabed environment. Such an extension is actually quite

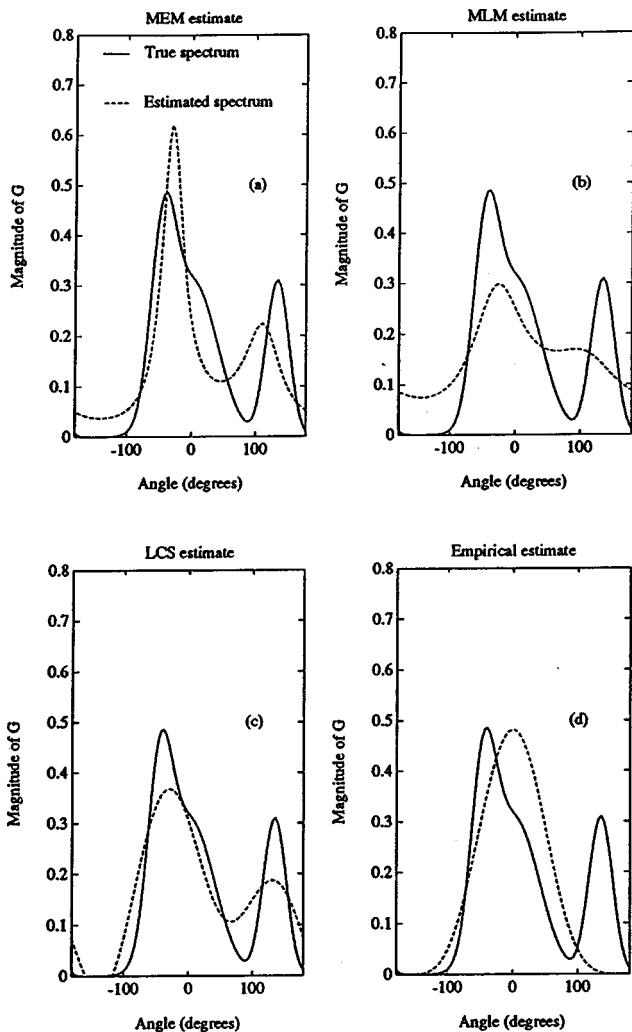


FIG. 9. Estimates of the directional spectrum of $G(\alpha) = N(\cos^8(\alpha/2) + \cos^{10}(\alpha/2 + \pi/4))$, where α is the azimuthal angle, and N is chosen to normalize the spectrum. The MEM estimate was made using the Lygre-Krogstad algorithm mentioned in the text. The MLM estimate was made using an algorithm by Lacoss (Ref. 35). The LCS estimate refers to the weighted average of the first five Fourier coefficients suggested by Longuet-Higgins *et al.* (Ref. 17). The empirical estimate was made by estimating the parameter s from the first five Fourier coefficients and using the empirical formula $G(\alpha) = N \cos^{2s}(\alpha/2)$.

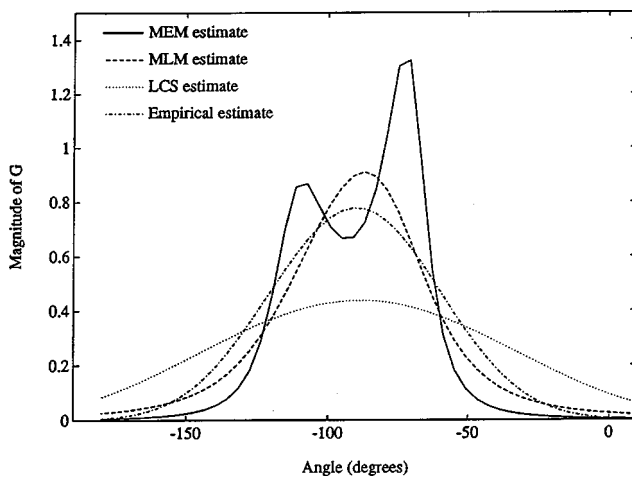


FIG. 10. Estimated spectra derived from the 0.16 Hz data bin from the Discus E buoy on January 27, 1991 at 1200 hours. The estimates were made using the methods discussed in Fig. 9.

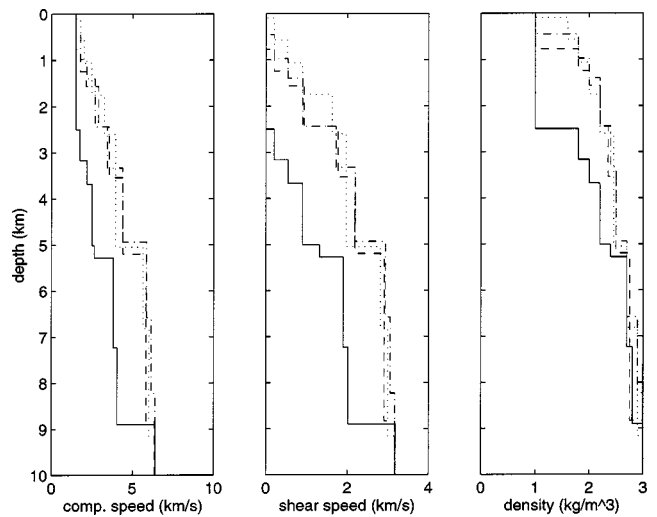


FIG. 11. Profiles used in the ULF/VLF noise model calculations. (a) Compressional wave speed. (b) Shear wave speed. (c) Density. Dotted line, 100 m water depth. Dashed line, 443 m water depth. Dash-dotted line, 769 m water depth. Solid line, 2600 m water depth.

straightforward when we realize the close relationship between Cato's coupling factors and the depth-dependent Green's functions often employed in ocean acoustics. First we make the observation, that, in Eq. (2), the factor $\exp(-i\omega r/c)/r$ is simply the free-space Green's function for a monopole, G_0 , which is the solution to

$$\frac{\partial^2 G_0}{\partial r^2} + (\omega/c)^2 G_0 = -4\pi\delta(\mathbf{r}). \quad (13)$$

In fact, for an ocean of infinite radius, Eq. (2) shows that the monopole coupling factor is proportional to the Hankel transform of the Green's function. Hence

$$H_0(\omega, k, z) = \frac{\omega}{2c} g_0(\omega, k, z), \quad (14)$$

where $g_0 = \int_0^\infty G_0(\omega, \hat{r}, z) J_0(k\hat{r}) \hat{r} d\hat{r}$ is the depth-dependent Green's function. From Eq. (7), it is evident that H_3 is proportional to the depth-dependent Green's function for a vertical dipole, $g_3 = \partial g_0 / \partial z$,

$$H_3(\omega, k, z) = \frac{1}{2} g_3(\omega, k, z). \quad (15)$$

Equations (1) and (3) can be interpreted physically as follows. To find the pressure spectrum in an infinitely deep ocean, one decomposes the Green's function for the appropriate source type into its horizontal wave number components by calculating the Hankel transform, takes the squared magnitude, multiplies by a source power proportional to the wave height power spectrum (or a convolution product) at each horizontal wave number, and then integrates over the horizontal wave number space. In fact, this procedure for calculating propagation from a surface distribution of noise sources has been given previously for *arbitrarily stratified* environments by Kuperman and Ingenito.²² Their Eq. (20) becomes, in our notation,

$$P(\omega, z) = \frac{\omega^2}{c^2} \int_{-\infty}^{\infty} \Pi(\mathbf{k}) |g(\omega, k, z)|^2 d\mathbf{k}, \quad (16)$$

where P is proportional to the acoustic intensity, Π is the power spectral density of the surface-distributed sources, and g is the depth-dependent Green's function. By setting $\Pi \propto \Psi_{33}$ for the monopoles, and $\Pi \propto \Phi_{i3j3} + \phi_{i33j}$ for the dipoles, it is recognized that Cato's theory provides the spectral density function for Kuperman and Ingenito's general equation for noise generated by surface-distributed sources in a horizontally stratified environment. Alternatively, Cato's expression for the acoustic fields carries over to the case of arbitrary stratification, so long as the appropriate depth-dependent Green's function is used. That is, we can continue to apply Eqs. (1) and (3) to arbitrarily stratified environments, while using Eqs. (14) and (15) to determine the coupling factors.²³

For the predictions in this paper, the ocean and underlying bottom were allowed to have depth-dependent compressional wave speed and attenuation, shear wave speed and attenuation, and density. The vertical profiles were piecewise constant. The depth-dependent Green's functions corresponding to these profiles were computed using a fast field program (FFP) written by Wilson,²⁴ which is based on the global-matrix algorithm developed by Schmidt and Tango.^{25,26} The FFP can also accommodate monopoles and dipoles that are positioned *on* (as opposed to just below or above) the air/sea interface; this capability is required for predicting the noise from sea-surface motion.

Once the depth-dependent Green's functions for the monopoles and dipoles have been determined by the FFP, they are multiplied by the appropriate forms of the surface-wave directional spectrum (Sec. II C 1) in accordance with Eqs. (1) and (3). The magnitude squared of the Green's function is multiplied by the source strength (surface-wave spectrum), and then integrated over the horizontal wave number space. The final result is pressure as a function of frequency and depth.

IV. ANALYSIS AND DISCUSSION

A. Comparison of the model and measurements

Model predictions, made with the methodology described in the preceding section, are shown in the lower panels of Figs. 4–7. The SWADE spectra usually had a low-frequency cutoff at 0.03 Hz and a high-frequency cutoff at 0.34 Hz (cf. Fig. 8). This limits the predictions for the single-frequency noise field to the frequency range 0.03–0.34 Hz, whereas the double-frequency predictions are limited to 0.06–0.68 Hz. Furthermore, the SWADE spectra were often unavailable at frequencies greater than the 0.03 Hz cutoff (due to difficulties associated with integrating accelerometer data to obtain wave height), thus causing a jagged edge on the low-frequency end of the spectra and further restricting the frequency range of the predictions.

Agreement between the data and the predictions is best for OBS 61, at 2600 m depth. For the most part, the magnitude and spectral shape of the experimental data are accurately predicted. There are cases, however, where the model predicts higher pressures than were measured (e.g., the storms occurring on yeardays 60–64), as well as cases where the model predicts lower pressures (e.g., the storms occur-

ring on yeardays 72–74 and 86–87). The likely causes are the low angular resolution of the surface-wave measurements, and the assumption of uniformity in the horizontal source distribution.

An interesting discrepancy between the predictions and the measurements occurs at the two intermediate depths (OBS's 63 and 62), in the frequency range of the double-frequency noise field. At these depths the predictions have a systematic bias not evident at OBS 61, being about 10 dB higher than the measured levels. This could be caused by the greater bottom slope at the intermediate depths, which may reflect some of the energy away from the continental slope region. (Recall that OBS 61 was located on the continental rise, whereas the other sensors were deployed on the steeper continental slope.) A more sophisticated propagation model incorporating lateral variability might successfully predict this trend.

The model successfully predicts the spectral gap between the single- and double-frequency noise at the intermediate depths, when SWADE data are available for sufficiently low frequencies. Like the double-frequency noise, the levels predicted for the single-frequency noise are somewhat high. However, the relative strengths of the single- and double-frequency noise are well predicted. At the shallowest sensor, OBS 51, the model predicts that a double-frequency noise with strong temporal variability should be evident above about 0.2 Hz. This is not borne out by the experimental spectra, though, which show little temporal variation on time scales associated with storm activity. The model also predicts a narrow spectral gap at slightly below 0.2 Hz, although no such gap is actually observed. During certain periods (e.g., yeardays 71–83), the OBS 51 data exhibit harmonics with spacing of about 0.1 Hz in the band 0.2–0.6 Hz. Kibblewhite and Wu²⁸ have suggested the existence of m th-frequency microseisms ($m > 2$), which, like the double-frequency microseisms, are produced by nonlinear interactions. Although Kibblewhite and Wu indicate that the m th-frequency microseisms will generally be negligible, they are perhaps evident in our data. Or, as pointed out by reviewers of this paper, the harmonics could be caused by shear-wave modes in the sediment or by nonlinear instrument response.

B. Effect of changing wave conditions on the double-frequency noise field

As discussed above, there is good overall agreement between the predicted spectral levels at most frequencies in the band of double-frequency microseisms. In this section we perform more detailed comparisons for selected times during ECONOMEX with differing wind and wave conditions.^{27,29}

Figure 12 shows an example of a case where there is particularly good agreement between the predictions and the measurements. The data are for OBS 61, the 2600 meter site. Figure 13 shows similar results at OBS 63, the 443 meter site. Shown with the spectra are the calculations of both the wave-height power spectrum $\Omega(\omega/2)$ and the spreading integral I_{33} from the appropriate SWADE data. While the predicted and observed levels at a given frequency may differ up to 5 dB, there is generally good correspondence between the two. It is interesting that in many of the comparisons

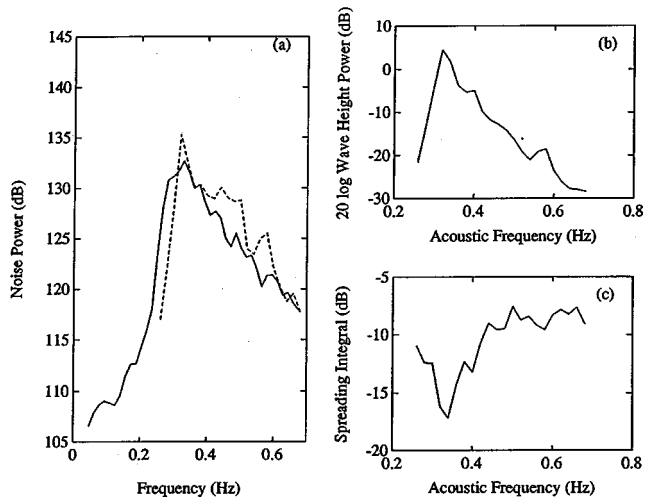


FIG. 12. (a) Observed (solid line) and predicted (dashed line) spectral levels for 1/27/91 at 1800 hours, in dB *re* 1 $\mu\text{Pa}^2/\text{Hz}$. Observed spectrum is from the OBS 58 differential pressure gauge (DPG). Predicted spectrum is based on data from the Discus E buoy. (b) Wave height power spectrum in dB, $10 \log \Omega^2(\omega/2)$, where $\Omega(\omega/2)$ has units m^2/Hz . (c) Spreading integral in dB, $10 \log I_{33}(\omega/2)$.

small peaks exist in the observed levels which are present in the predictions at the same frequencies but with different magnitudes. One can see from the inputs that the spreading integral plays a key role in determining the shape and magnitude of the predicted spectra. These two figures represent particularly good agreement between predicted and observed spectra.

More typical of the level of agreement are Figs. 14 and 15, where we can see close agreement at frequencies around the spectral peak, but differences away from the peak of 5 or more dB is sometimes evident. In general, the overall spectral shape is correctly predicted, but the peak is broader or narrower in the observed spectra, giving rise to large differences in the high-slope region on the low-frequency side of the peak. In the predictions from the shallow site, there is a

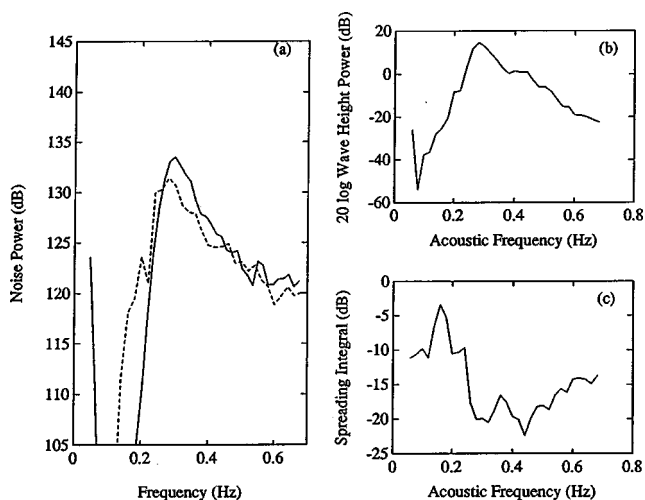


FIG. 13. (a) Observed (solid line) and predicted (dashed line) spectral levels of 2/23/91 at 1400 hours, in dB *re* 1 $\mu\text{Pa}^2/\text{Hz}$. Observed spectrum is from the OBS 63 DPG. Predicted spectrum is based on data from the Discus C buoy. (b) Wave height power spectrum in dB, $10 \log \Omega^2(\omega/2)$, where $\Omega(\omega/2)$ has units m^2/Hz . (c) Spreading integral in dB, $10 \log I_{33}(\omega/2)$.

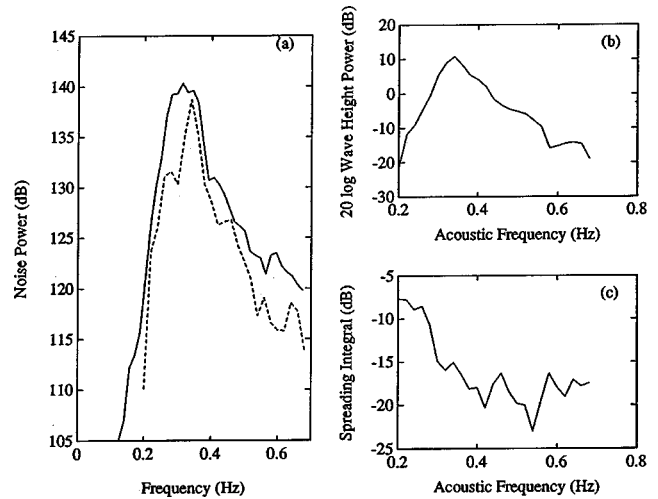


FIG. 14. (a) Observed (solid line) and predicted (dashed line) spectral levels for 2/23/91 at 0700 hours, in dB *re* 1 $\mu\text{Pa}^2/\text{Hz}$. Observed spectrum is from the OBS 58 DPG. Predicted spectrum is based on data from the Discus E buoy. (b) Wave height power spectrum in dB, $10 \log \Omega^2(\omega/2)$, where $\Omega(\omega/2)$ has units m^2/Hz . (c) Spreading integral in dB, $10 \log I_{33}(\omega/2)$.

tendency to predict levels that are too high in the band 0.1 Hz to 0.2 Hz. Since this band corresponds to the peak in the bottom response in the shallow case, errors in the bottom model may account for this difference.

The observations show an increase in noise level with wave height, and good agreement between observations and predictions at moderate (~ 1 to 3 m) wave heights is evident in Figs. 12–15. At very low predicted noise levels, which correspond to times of low wave height, there is a disparity between predictions and observations. An example of this is the developing wave field of the early hours of January 27 at Discus E, as depicted in Fig. 16. As one can see in Figs. 17 and 18, agreement is good at frequencies corresponding to the peak in the predictions as the wave field develops, but the low levels predicted away from the peak are not confirmed by observation. A possible cause of the error in the predic-

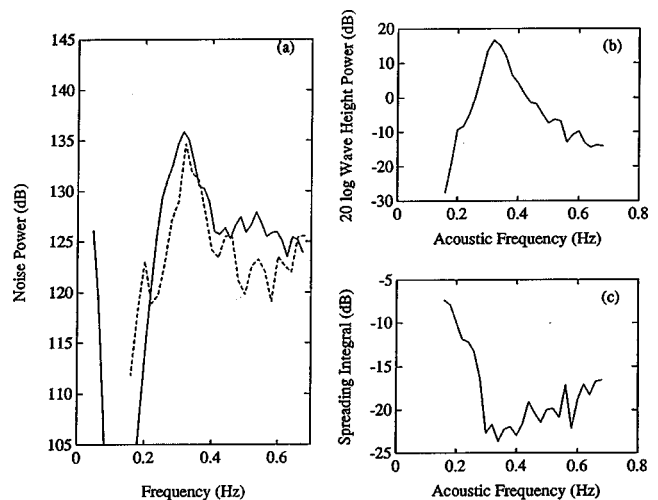


FIG. 15. (a) Observed (solid line) and predicted (dashed line) spectral levels for 2/27/91 at 1500 hours, in dB *re* 1 $\mu\text{Pa}^2/\text{Hz}$. Observed spectrum is from the OBS 63 DPG. Predicted spectrum is based on data from the Discus C buoy. (b) Wave height power spectrum in dB, $10 \log \Omega^2(\omega/2)$, where $\Omega(\omega/2)$ has units m^2/Hz . (c) Spreading integral in dB, $10 \log I_{33}(\omega/2)$.

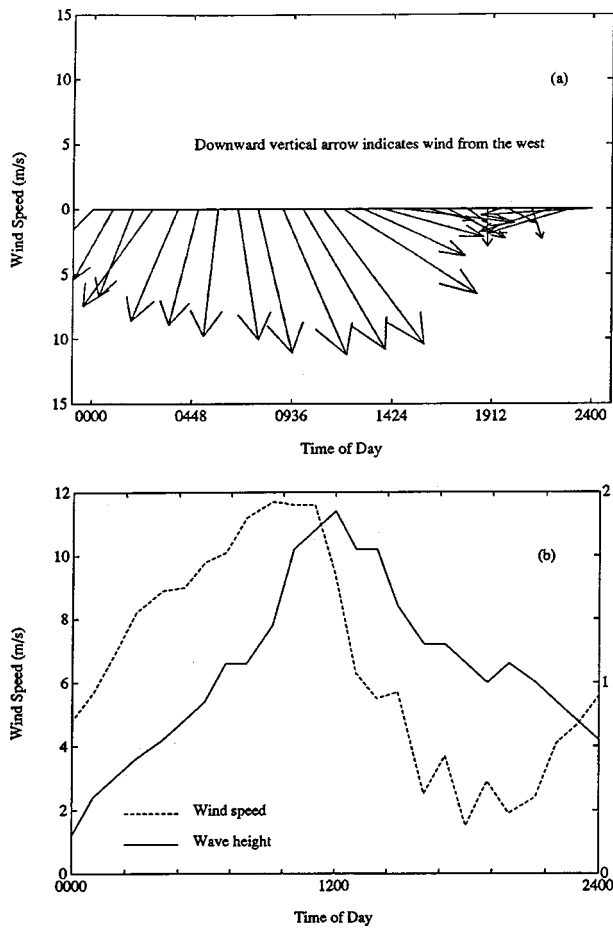


FIG. 16. Meteorological data as measured at Discus E on 1/27/91. (a) Wind vector. The direction of the arrow indicates the direction of the wind, with a downward arrow indicating a wind from the west. The magnitude of the arrow indicates the wind speed with the wind speed scale given on the vertical axis. (b) Wind speed and wave height.

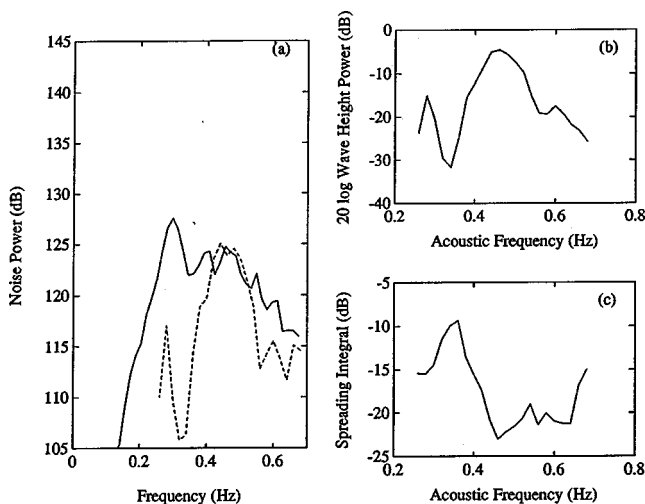


FIG. 17. (a) Observed (solid line) and predicted (dashed line) spectral levels for 1/27/91 at 0600 hours, in dB *re* $1 \mu\text{Pa}^2/\text{Hz}$. Observed spectrum is from the OBS 58 DPG. Predicted spectrum is based on data from the Discus E buoy. (b) Wave height power spectrum in dB, $10 \log \Omega^2(\omega/2)$, where $\Omega(\omega/2)$ has units m^2/Hz . (c) Spreading integral in dB, $10 \log I_{33}(\omega/2)$.

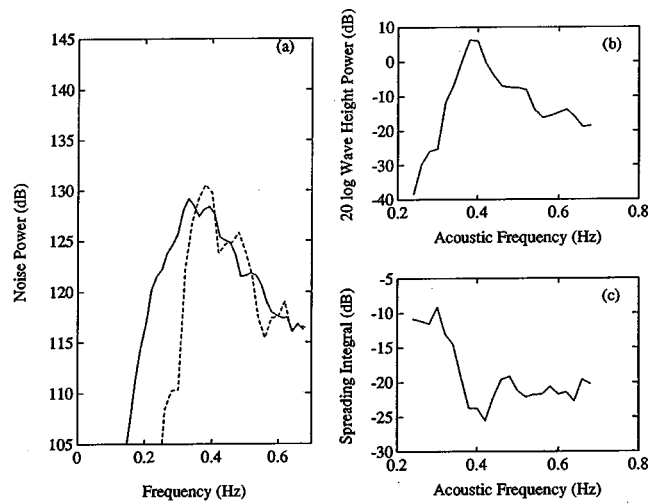


FIG. 18. (a) Observed (solid line) and predicted (dashed line) spectral levels for 1/27/91 at 0900 hours, in dB *re* $1 \mu\text{Pa}^2/\text{Hz}$. Observed spectrum is from the OBS 58 DPG. Predicted spectrum is based on data from the Discus E buoy. (b) Wave height power spectrum in dB, $10 \log \Omega^2(\omega/2)$, where $\Omega(\omega/2)$ has units m^2/Hz . (c) Spreading integral in dB, $10 \log I_{33}(\omega/2)$.

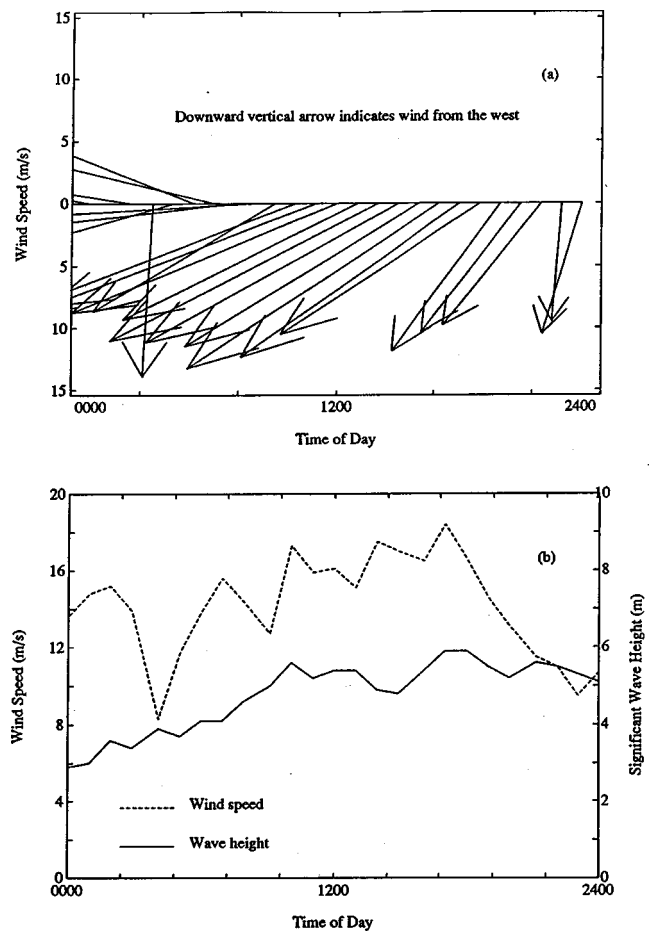


FIG. 19. Meteorological data as measured at Discus E on 3/04/91. (a) Wind vector. The direction of the arrow indicates the direction of the wind, with a downward arrow indicating a wind from the west. The magnitude of the arrow indicates the wind speed with the wind speed scale given on the vertical axis. (b) Wind speed and wave height.

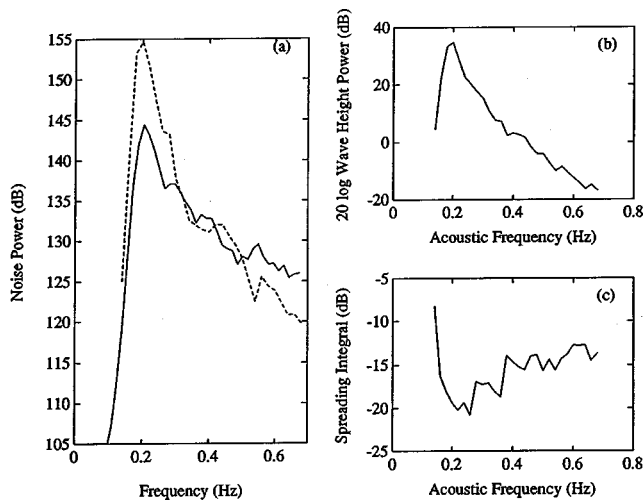


FIG. 20. (a) Observed (solid line) and predicted (dashed line) spectral levels for 3/04/91 at 1000 hours, in dB *re* $1 \mu\text{Pa}^2/\text{Hz}$. Observed spectrum is from the OBS 58 DPG. Predicted spectrum is based on data from the Discus E buoy. (b) Wave height power spectrum in dB, $10 \log \Omega^2(\omega/2)$, where $\Omega(\omega/2)$ has units m^2/Hz . (c) Spreading integral in dB, $10 \log I_{33}(\omega/2)$.

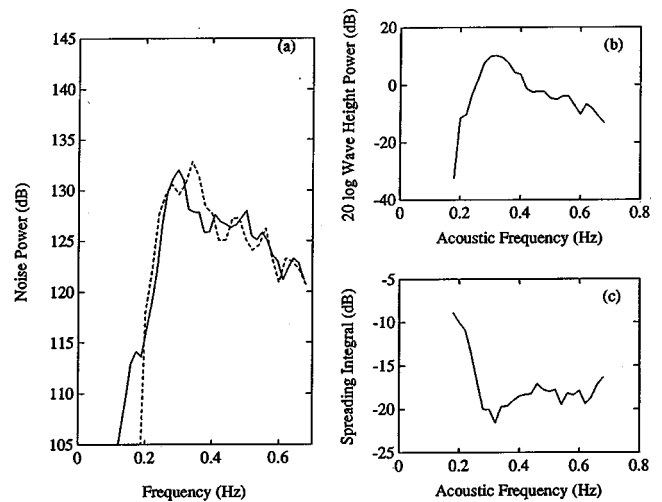


FIG. 22. (a) Observed (solid line) and predicted (dashed line) spectral levels for 2/23/91 at 0300 hours, in dB *re* $1 \mu\text{Pa}^2/\text{Hz}$. Observed spectrum is from the OBS 58 DPG. Predicted spectrum is based on data from the Discus E buoy. (b) Wave height power spectrum in dB, $10 \log \Omega^2(\omega/2)$, where $\Omega(\omega/2)$ has units m^2/Hz . (c) Spreading integral in dB, $10 \log I_{33}(\omega/2)$.

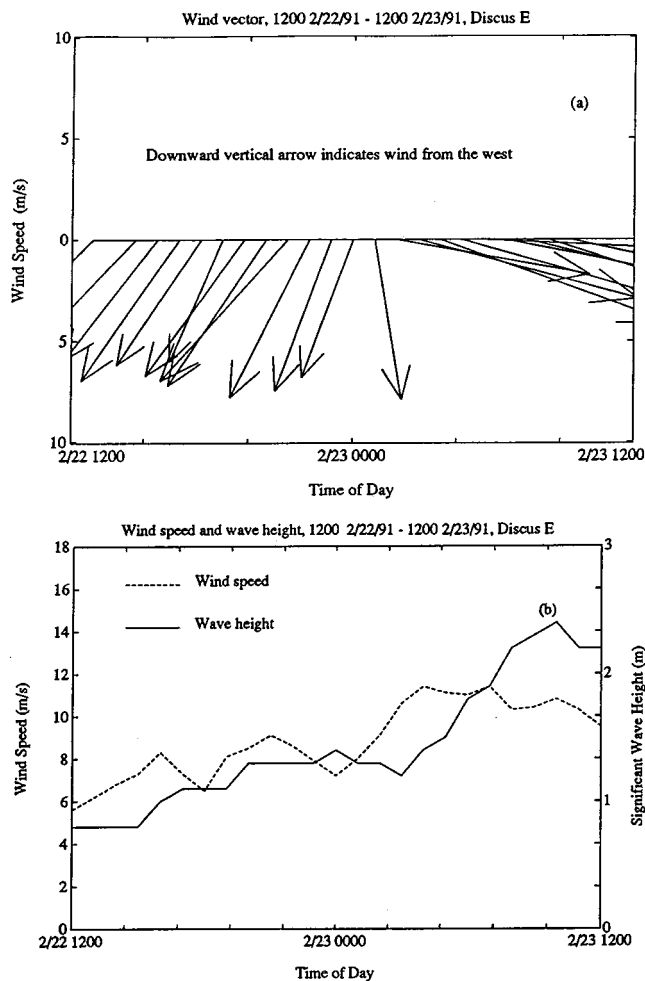


FIG. 21. Meteorological data as measured at Discus E on 2/22/91–2/23/91. (a) Wind vector. The direction of the arrow indicates the direction of the wind, with a downward arrow indicating a wind from the west. The magnitude of the arrow indicates the wind speed with the wind speed scale given on the vertical axis. (b) Wind speed and wave height.

tions at low wave heights is the assumption of spatial homogeneity of the source wave field. Under very low local wave height conditions, it is possible for a much stronger wave field at some distance to dominate the noise field, thus making the predictions made from the local wave field very much in error. Another possible cause of the differences under low wave height conditions is the existence of an unknown source mechanism generating acoustic energy, whose noise is normally dominated by that caused by orbital motion. Under low source strength conditions for the orbital motion noise, this presumed source may now dominate, giving rise to the errors noted above. The predictions in general are in reasonably close agreement when measured significant wave height is above about 1 meter. For the period of the ECONOMEX data, roughly 77% of the wave height measurements are above this threshold.

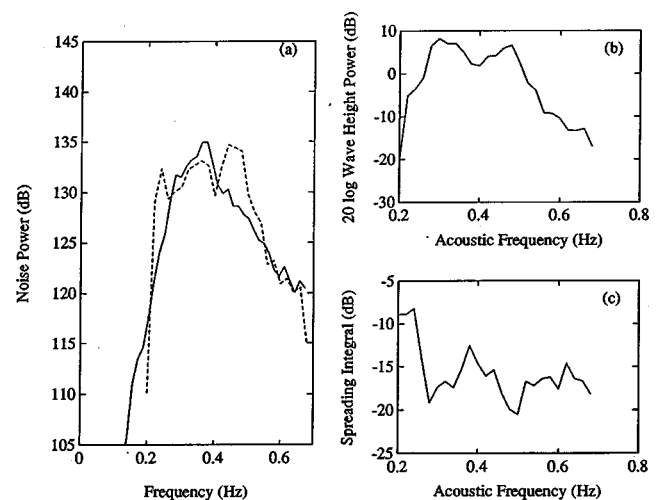


FIG. 23. (a) Observed (solid line) and predicted (dashed line) spectral levels for 2/23/91 at 0400 hours, in dB *re* $1 \mu\text{Pa}^2/\text{Hz}$. Observed spectrum is from the OBS 58 DPG. Predicted spectrum is based on data from the Discus E buoy. (b) Wave height power spectrum in dB, $10 \log \Omega^2(\omega/2)$, where $\Omega(\omega/2)$ has units m^2/Hz . (c) Spreading integral in dB, $10 \log I_{33}(\omega/2)$.

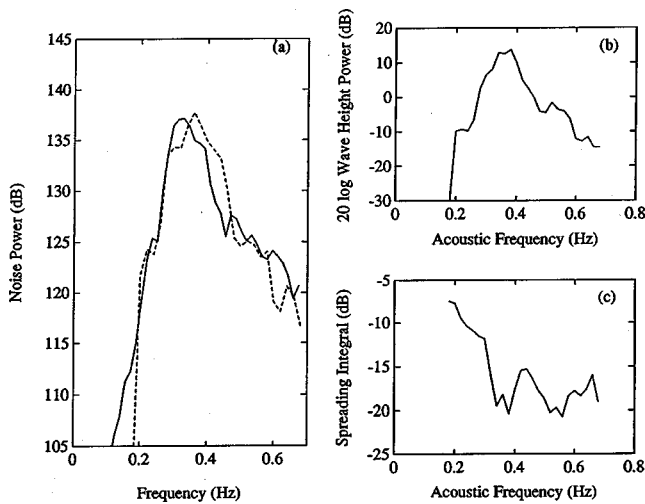


FIG. 24. (a) Observed (solid line) and predicted (dashed line) spectral levels for 2/23/91 at 0500 hours, in dB *re* $1 \mu\text{Pa}^2/\text{Hz}$. Observed spectrum is from the OBS 58 DPG. Predicted spectrum is based on data from the Discus E buoy. (b) Wave height power spectrum in dB, $10 \log \Omega^2(\omega/2)$, where $\Omega(\omega/2)$ has units m^2/Hz . (c) Spreading integral in dB, $10 \log I_{33}(\omega/2)$.

We can see from the data of March 4 (with meteorological conditions shown in Fig. 19 and observed and predicted spectra seen in Fig. 20) that the predictions again deviate at very high wave height conditions corresponding to strong winds at relatively constant direction, with the predictions being higher than the observations. The disagreement at frequencies corresponding to the peak is up to 10 dB under these conditions. There is, however, the same general trend in the observed noise data as exists in the predictions, that of higher levels at higher wave heights and wind speeds. This would tend to indicate the wave directional spectral estimate provided by the MEM technique is overestimating the spreading at these high wave heights. Alternative empirical models, which are based on strong, steady winds, predict less spreading under these conditions than do the MEM estimates (Fig. 9). The observations match the predictions fairly well

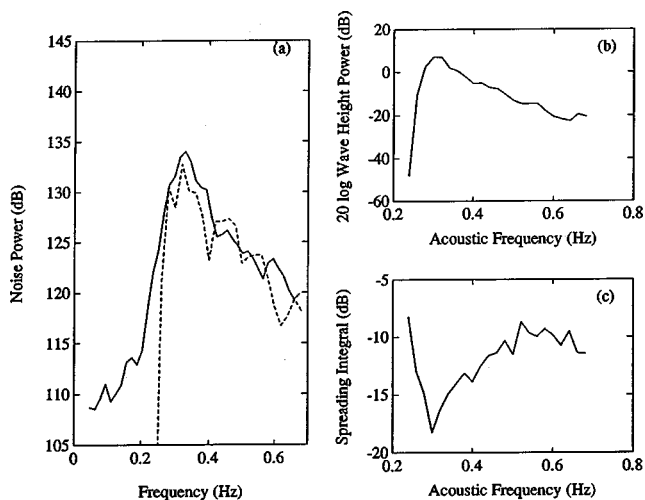


FIG. 25. (a) Observed (solid line) and predicted (dashed line) spectral levels for 1/27/91 at 1500 hours, in dB *re* $1 \mu\text{Pa}^2/\text{Hz}$. Observed spectrum is from the OBS 58 DPG. Predicted spectrum is based on data from the Discus E buoy. (b) Wave height power spectrum in dB, $10 \log \Omega^2(\omega/2)$, where $\Omega(\omega/2)$ has units m^2/Hz . (c) Spreading integral in dB, $10 \log I_{33}(\omega/2)$.

in the region of frequencies above the peak under high wave height conditions.

The predictions agree quite well with the observed data under conditions of changing wind direction. We can consider the wind shift of February 23 at 0200, depicted in Fig. 21, as typical. The observed and predicted noise levels for subsequent times are shown in Figs. 22–24. The observed noise spectrum changes with time roughly as the predicted spectrum does. Of particular note is the broad peak in the observed spectrum at 0400, and the higher levels seen at the peak from 0300–0500. Again the spreading integral plays a major role in determining the spectral shape.

It is also interesting to examine the predictions and observations during a time of highly variable conditions such as those of the afternoon of January 27, which were depicted in Fig. 16. Observations and predictions are seen in Figs. 12 and 25, for 1800 and 1500, respectively. Again we see relatively close agreement, with the increased spreading adding to the noise as the wave height diminishes to keep the overall noise level fairly constant.

V. CONCLUSIONS

ECONOMEX has provided a unique opportunity to compare ULF noise spectra recorded in different water depths over a 10 week period. The experimental results, and the accompanying model predictions, clearly demonstrate that surface-wave orbital motion is the primary cause of noise in the frequency band 0.02–2 Hz. The fact that the model predictions hold well under conditions of changing wind direction, for which the double-frequency noise is enhanced, demonstrates that wind turbulence acting on the sea surface (which would depend on the wind speed but not the direction) is not a significant mechanism of ULF/VLF sound generation.

The surface-wave motion generates noise via two distinct mechanisms. These are referred to as single- and double-frequency noise fields. The former is due to linearly generated pressure fluctuations following a single surface wavetrain, while the latter results from nonlinear interaction between opposing surface wavetrains. Both mechanisms are clearly evident in the ECONOMEX data.

The single-frequency noise field is strongest at the shallowest sensor (95 m). Levels as high as 160 dB *re* $1 \mu\text{Pa}^2/\text{Hz}$ were measured, and there appears to be generation of higher harmonics by finite amplitude effects. The intensity and peak frequency of the single-frequency noise decreases rapidly with depth, as would be expected. The single-frequency noise exhibits little temporal variability, relative to the surface wave spectra.

The double-frequency noise field is observed at all depths and exhibits little depth dependence. Also, unlike the single-frequency counterpart, the temporal variations in the double-frequency noise closely track the surface-wave spectra, except at the shallowest sensor. Because the peak frequency of the single-frequency noise diminishes with depth, whereas the peak of the double-frequency noise is relatively constant, a spectral gap whose width increases with depth is observed.

Most features of the data are well predicted by the theory of Cato,^{2,3} which we have extended to accommodate a horizontally stratified ocean and seabed. Some of the discrepancies between the data and predictions may be attributable to lateral variability in the environment, particularly since the experiment was performed in a continental shelf/slope region. More sophisticated modeling efforts, accounting for lateral variation in the ocean and seabed as well as the source function (i.e., the surface-wave field), should improve agreement with the data.

The importance of the wave-directional spectrum in determining the overall noise level is apparent from this study. Any models based on empirical relationships using wind speed as their input would have to also include the growth and decay of the wave field resulting from changing wind direction. Models that predict directional wave spectra from a knowledge of wind speed alone are doomed to failure in general, due to their assumption of a fully developed wave field, and to the changing nature of the true wave field.

This work has also demonstrated the key role played by the propagation environment, particularly the geoacoustic bottom model, in determining the overall levels and shape of the acoustic noise spectrum at extremely low frequencies. This observation is consistent with the work of Schmidt and Kuperman.³⁰ Hence it is imperative that the propagation environment be taken into account if one wishes to compare actual source levels between two different locations. Otherwise differences in the bottom site characteristics could cloud important correlations or lead to incorrect conclusions.

ACKNOWLEDGMENTS

This work was supported by Office of Naval Research Grant No. N00014-90-J-1452, G. M. Purdy and G. V. Fisk, Co-Principal Investigators. They gratefully acknowledge the assistance of the crew of the R/V Oceanus in the acquisition of the data. D. K. Wilson was also supported by a post-doctoral scholarship from the WHOI Education Office. The authors thank J. Collins, D. DuBois, and G. M. Purdy for providing the OBS data in SEG Y format, and S. Holbrook for providing the EDGE data. We also thank G. H. Sutton for many helpful discussions. This paper is WHOI Contribution No. 10893.

APPENDIX: DETERMINATION OF THE SURFACE-WAVE DIRECTIONAL SPECTRUM

In this Appendix we consider the angular resolution available from the SWADE Discus buoys. Longuet-Higgins *et al.*¹⁷ were the first to investigate the angular response of such pitch and roll buoys. They pointed out that if the wavelengths of the sea surface motion are large with respect to the buoy diameter, the buoy tends to have the same motion and orientation as the surface. Then, if the vertical displacement and the two angles of pitch and roll are measured, one has three time series: the vertical displacement ζ , and its spatial derivatives $\partial\zeta/\partial x$ and $\partial\zeta/\partial y$. We denote these three quantities as ξ_1 , ξ_2 , and ξ_3 , respectively, in the following discussion.

The vertical displacement may be represented using the following stochastic integral:

$$\xi_1 = \text{Re} \int_S \exp[i(k_x x + k_y y - \omega t)] d\mathbf{S}. \quad (\text{A1})$$

Then, since $(k_x, k_y) = (k \cos \alpha, k \sin \alpha)$, we can write our other two time series as

$$\xi_2 = \text{Re} \int_S i k \cos \alpha \exp[i(k_x x + k_y y - \omega t)] d\mathbf{S}, \quad (\text{A2})$$

$$\xi_3 = \text{Re} \int_S i k \sin \alpha \exp[i(k_x x + k_y y - \omega t)] d\mathbf{S}.$$

Next we form co-spectra $C_{ij}(\omega)$ and quadrature spectra $Q_{ij}(\omega)$ from the time series ξ_i and ξ_j , finding

$$\begin{aligned} C_{11}(\omega) &= \int_0^{2\pi} F(\omega, \alpha) d\alpha, \\ C_{22}(\omega) &= \int_0^{2\pi} k^2 \cos^2 \alpha F(\omega, \alpha) d\alpha, \\ C_{33}(\omega) &= \int_0^{2\pi} k^2 \sin^2 \alpha F(\omega, \alpha) d\alpha, \\ C_{23}(\omega) &= \int_0^{2\pi} k^2 \cos \alpha \sin \alpha F(\omega, \alpha) d\alpha, \\ Q_{12}(\omega) &= \int_0^{2\pi} k \cos \alpha F(\omega, \alpha) d\alpha, \\ Q_{13}(\omega) &= \int_0^{2\pi} k \sin \alpha F(\omega, \alpha) d\alpha, \end{aligned} \quad (\text{A3})$$

where $F(\omega, \alpha) = \Omega(\omega)G(\omega, \alpha)$ is the frequency-directional spectrum of the sea surface elevation. The Fourier coefficients of $F(\omega, \alpha)$ are defined as

$$a_n(\omega) + i b_n(\omega) = \frac{1}{\pi} \int_0^{2\pi} e^{in\alpha} F(\omega, \alpha) d\alpha, \quad (\text{A4})$$

where

$$F(\omega, \alpha) = \frac{1}{2} a_0 + \sum_{n=1}^{n=\infty} [a_n \cos(n\alpha) + b_n \sin(n\alpha)]. \quad (\text{A5})$$

Now we can see that the right-hand sides of Eq. (A3) are related to these Fourier coefficients as follows:

$$\begin{aligned} a_0(\omega) &= \frac{1}{\pi} C_{11}(\omega), \\ a_1(\omega) &= \frac{1}{\pi k} Q_{12}(\omega), \quad b_1(\omega) = \frac{1}{\pi k} Q_{13}(\omega), \\ a_2(\omega) &= \frac{1}{\pi k^2} [C_{22}(\omega) - C_{33}(\omega)], \quad b_2(\omega) = \frac{2}{\pi k^2} C_{23}(\omega). \end{aligned} \quad (\text{A6})$$

The pitch and roll buoy hence provides the first five coefficients in the Fourier series describing the directional spectrum of the sea surface elevation, each coefficient being a function of frequency ω . We must now use these five Fourier coefficients to find estimates of the wave-height power spectrum $\Omega(\omega)$ and the directionality function $G(\omega, \alpha)$.

Our estimate of the wave-height power spectrum is obvious from inspection of Eq. (A5) and our definition of the co-spectra:

$$\Omega(\omega) = \int_0^{2\pi} F(\omega, \alpha) d\alpha = \pi a_0(\omega) = C_{11}(\omega). \quad (\text{A7})$$

The best estimate for the directional spectrum is not as simple. An obvious choice would be to try the truncated sum

$$G(\omega, \alpha) = \frac{1}{2\pi} + \frac{1}{\pi a_0} (a_1 \cos \alpha + b_1 \sin \alpha + a_2 \cos 2\alpha + b_2 \sin 2\alpha). \quad (\text{A8})$$

This sum is actually a convolution of the true directional spectrum with a weighting function, and considerable smoothing results in the estimated spectrum. Unfortunately, calculations of the spreading integral, I_{33} [Eq. (9)], made using this type of directional spectrum estimate can be shown to be in error by factors as large as 10^3 .²⁷ Other weighted averages of the first five Fourier coefficients can be made, but they also produce an unrealistically smooth estimate.

Several investigators have fit empirical curves to measured directional spectra. Longuet-Higgins *et al.* have suggested the wave directional spectra fit the form¹⁷

$$G(\omega, \alpha) \propto |\cos^{2s}(\alpha/2)| \quad (\text{A9})$$

where the spreading parameter s is a function of frequency and wind speed. Kibblewhite and Wu³¹ used an empirical relationship to find s based on the wind speed and frequency, and then calculated I_{33} analytically. One could also match the measured first five Fourier coefficients to the first five Fourier coefficients of the empirical spectrum $\cos^{2s} \alpha/2$ to estimate the parameter s , as suggested by Longuet-Higgins *et al.*,¹⁷ and hence calculate I_{33} . However, the data used to develop the empirical formula are generally taken under conditions of steady wind speed and direction. In our field data, the wind speed and direction can vary significantly, giving rise to wave fields with different directionality, and in general a broader directional spectrum than that predicted by the empirical formula. Therefore, we would expect predictions of I_{33} calculated from spectra derived from empirical formulas to be lower than the true value under variable meteorological conditions. In particular, if the true directional spectrum is bi-directional (two peaks corresponding to two wave fields generated by winds in different directions) there can be significant energy in opposing wave directions which is not predicted by the cosine power curve. Donelan *et al.*³² have suggested a better fit to the data is found in a $\text{sech}^2 \beta \alpha$ distribution with β being the spreading parameter, but estimates of I_{33} based on estimates of β are also too small.

Another approach would be to use a data adaptive spectral estimation technique such as the maximum-likelihood method (MLM), or the maximum-entropy method (MEM). These methods have the common characteristic that the first five Fourier coefficients of the directional spectrum are used to estimate the remaining ones. The MEM technique has been shown by Lygre and Krogstad³³ to give a much more peaked distribution than the MLM technique, and also re-

solves bi-directional wavefields more satisfactorily. (Examples were given in Sec. II C 1.) Both of these features of the MEM technique are important for accurate calculations of the spreading integral. Hence MEM should give the best results in our application.

Our algorithm for producing MEM estimates largely follows Lygre and Krogstad.³³ We begin by defining a Fourier series for the directional spectrum $G(\alpha)$ (suppressing for now the dependence on ω) on the interval $(-\pi, \pi)$ as

$$G(\alpha) = \frac{1}{2\pi} \sum_{n=-\infty}^{\infty} c_n e^{in\alpha}, \quad c_0 = 1, \quad c_{-n} = c_n^*. \quad (\text{A10})$$

The entropy of G is defined by

$$H(G) = 1 \left/ \int_{-\pi}^{\pi} \log(G(\alpha)) d\alpha \right. \quad (\text{A11})$$

It has been shown by Burg³⁴ that the function maximizing $H(G)$ subject to the constraint that the coefficients c_n equal some known c_k for $k \leq N$ is

$$G(\alpha) = \frac{1}{2\pi} \frac{\theta_e^2}{|1 - \phi_1 e^{-i\alpha} - \dots - \phi_N e^{-iN\alpha} G|^2}, \quad (\text{A12})$$

where $\phi_1 \dots \phi_N$ and θ_e^2 are obtained from the Yule-Walker equations

$$\begin{bmatrix} 1 & c_1^* & \dots & c_{N-1}^* \\ c_1 & \ddots & \ddots & \vdots \\ \vdots & \ddots & \ddots & c_1^* \\ c_{N-1} & \dots & c_1 & 1 \end{bmatrix} \times \begin{bmatrix} \phi_1 \\ \vdots \\ \phi_N \end{bmatrix} = \begin{bmatrix} c_1 \\ \vdots \\ c_N \end{bmatrix}, \quad (\text{A13})$$

and

$$\theta_e^2 = 1 - \phi_1 c_1^* - \dots - \phi_N c_N^*. \quad (\text{A14})$$

In our case we have $N=2$ with $c_1 = (a_1 - ib_1)/a_0$ and $c_2 = (a_2 - ib_2)/a_0$. We can now solve this system of equations to find ϕ_n in terms of c_n ,

$$\begin{aligned} \phi_1 &= (c_1 - c_2 c_1^*) / (1 - |c_1|^2), \\ \phi_2 &= c_2 - c_1 \phi_1. \end{aligned} \quad (\text{A15})$$

Finally, we can substitute these into Eq. (A12) to find our directional spectral estimate

$$G(\alpha) = \frac{1 - \phi_1 c_1^* - \phi_2 c_2^*}{2\pi |1 - \phi_1 e^{-i\alpha} - \phi_2 e^{2i\alpha}|^2}. \quad (\text{A16})$$

We now have an estimate of the angular distribution of the wave energy at each frequency which reproduces the first five Fourier coefficients, and uses these coefficients and the Yule-Walker equations to extrapolate the remaining coefficients.

¹M. S. Longuet-Higgins, "A theory of the origin of microseisms," *Philos. Trans. R. Soc. London, Ser. A* **243**, 1–35 (1950).

²D. H. Cato, "Sound generation in the vicinity of the sea surface: Source mechanisms and the coupling to the received sound field," *J. Acoust. Soc. Am.* **89**, 1076–1095 (1991).

³D. H. Cato, "Theoretical and measured underwater noise from surface wave orbital motion," *J. Acoust. Soc. Am.* **89**, 1096–1112 (1991).

⁴R. H. Nichols, "Infrasound ambient ocean noise measurements: Eleuthera," *J. Acoust. Soc. Am.* **69**, 974–981 (1981).

- ⁵T. E. Talpey and R. D. Worley, "Infrasonic ambient noise measurements in deep Atlantic water," *J. Acoust. Soc. Am.* **75**, 621–622 (1984).
- ⁶R. G. Adair, J. A. Orcutt, and T. H. Jordan, "Low-frequency noise observations in the deep ocean," *J. Acoust. Soc. Am.* **80**, 633–645 (1986).
- ⁷G. H. Sutton and N. Barstow, "Ocean-bottom ultralow-frequency (ULF) seismo-acoustic ambient noise: 0.002 to 0.4 Hz," *J. Acoust. Soc. Am.* **87**, 2005–2011 (1990).
- ⁸S. C. Webb and C. S. Cox, "Observations and modeling of seafloor microseisms," *J. Geophys. Res., [Oceans]* **91**, 7343–7358 (1986).
- ⁹A. C. Kibblewhite and K. C. Ewans, "Wave-wave interactions, microseisms, and infrasonic ambient noise in the ocean," *J. Acoust. Soc. Am.* **78**, 981–994 (1985).
- ¹⁰J. M. Babcock, B. A. Kirkendall, and J. A. Orcutt, "Relationships between ocean-bottom noise and the environment," *Bull. Seismol. Soc. Am.* **84**, 1991–2007 (1994).
- ¹¹T. Nye and T. Yamamoto, "Concurrent measurements of the directional spectra of microseismic energy and surface gravity-waves," *J. Geophys. Res., [Oceans]* **99**(C7), 14321–14338 (1994).
- ¹²T. H. C. Herbers and R. T. Guza, "Nonlinear wave interactions and high-frequency sea-floor pressure," *J. Geophys. Res., [Oceans]* **99**(C5), 10035–10048 (1994).
- ¹³C. T. Tindle and M. J. Murphy, "Microseisms and ocean wave measurements," *IEEE J. Ocean. Eng.* **24**, 112–115 (1999).
- ¹⁴S. C. Webb, "Broadband seismology and noise under the ocean," *Rev. Geophys.* **36**, 105–142 (1998).
- ¹⁵R. A. Weller, M. A. Donelan, M. G. Briscoe, and N. E. Huang, "Riding the crest: a tale of two experiments," *Bull. Am. Meteorol. Soc.* **72**, 163–183 (1991).
- ¹⁶R. E. Sheridan, D. L. Musser, L. Glover III, M. Talwani, J. Ewing, S. Holbrook, G. M. Purdy, R. Hawman, and S. Smithson, "EDGE deep seismic reflection study of the U.S. mid-Atlantic continental margin," *EOS Trans. Am. Geophys. Union* **72**, 273–274 (1991).
- ¹⁷M. S. Longuet-Higgins, D. E. Cartwright, and N. D. Smith, "Observations of the directional spectrum of sea waves using the motions of a floating buoy," *Ocean Wave Spectra* (Prentice-Hall, Englewood Cliffs, NJ, 1963).
- ¹⁸G. M. Purdy, L. Dorman, A. Schultz, and S. C. Solomon, "An ocean bottom seismometer for the Office of Naval Research," in *ULF/VLF (0.001 to 50 Hz) seismo-acoustic noise in the ocean*, Proceedings of a workshop at the Institute for Geophysics, University of Texas, Austin, November 29 to December 1, 1988, edited by G. H. Sutton (Office of Naval Research, Arlington, VA, 1990).
- ¹⁹E. L. Hamilton, "Geoacoustic modeling of the sea floor," *J. Acoust. Soc. Am.* **68**, 1313–1340 (1980).
- ²⁰S. Holbrook (private communication).
- ²¹J. Ewing (private communication).
- ²²W. A. Kuperman and F. Ingenito, "Spatial correlation of surface generated noise in a stratified ocean," *J. Acoust. Soc. Am.* **67**, 1988–1996 (1980).
- ²³Our method for predicting noise generated by surface waves, as presented in the text, is valid for stratified environments having infinite horizontal extent. By implication the source distribution also has infinite extent. In this regard our model is less general than Cato's (Ref. 2), who modeled the ocean as a semi-infinite cylinder with finite radius.
- ²⁴D. K. Wilson, "Sound field computations in a stratified, moving medium," *J. Acoust. Soc. Am.* **94**, 400–407 (1993).
- ²⁵H. Schmidt and G. Tango, "Efficient global matrix approach to the computation of synthetic seismograms," *Geophys. J. R. Astron. Soc.* **84**, 331–359 (1986).
- ²⁶H. Schmidt, *SAFARI: Seismo-Acoustic Fast Field Algorithm for Range Independent Environments. User's Guide* (SACLANT ASW Research Centre, La Spezia, Italy, 1986), SR 113.
- ²⁷T. E. Lindstrom, "Predictions and observations of seafloor infrasonic noise generated by sea surface orbital motion," Ocean Engineer dissertation, Massachusetts Institute of Technology and Woods Hole Oceanographic Institution, 1991.
- ²⁸A. C. Kibblewhite and C. Y. Wu, "The theoretical description of wave-wave interactions as a noise source in the ocean," *J. Acoust. Soc. Am.* **89**, 2241–2252 (1991).
- ²⁹The method used to make the theoretical predictions in Sec. IV B is described by Lindstrom (Ref. 27). Lindstrom's method is very similar, but not identical, to the one described in Sec. III. The latter incorporates some corrections for calculation of the effects of the depth-dependent ocean environment on the propagation. However, these corrections affect only the time-independent transfer function between the surface waves and the bottom-based sensors; the time-varying effects of the wave height spectrum and spreading are the same in both models. Therefore the differences between the two methods do not significantly affect the conclusions in Sec. IV B.
- ³⁰H. Schmidt and W. A. Kuperman, "Estimation of surface noise source level from low-frequency seismoacoustic ambient noise measurements," *J. Acoust. Soc. Am.* **84**, 2153–2162 (1988).
- ³¹A. C. Kibblewhite and C. Y. Wu, "The generation of infrasonic ambient noise in the ocean by nonlinear interactions of ocean surface waves," *J. Acoust. Soc. Am.* **85**, 1935–1945 (1989).
- ³²M. A. Donelan, J. Hamilton, and W. H. Hui, "Directional spectra of wind-generated waves," *Philos. Trans. R. Soc. London, Ser. A* **315**, 509–562 (1985).
- ³³A. Lygre and H. E. Krogstad, "Maximum entropy estimation of the directional distribution in ocean wave spectra," *J. Phys. Oceanogr.* **16**, 2052–2060 (1986).
- ³⁴J. P. Burg, "Maximum entropy spectral analysis," Ph.D. dissertation, Stanford University, 1976.
- ³⁵R. T. Lacoss, "Data adaptive spectral analysis methods," *Geophysics* **36**, 661–675 (1971).